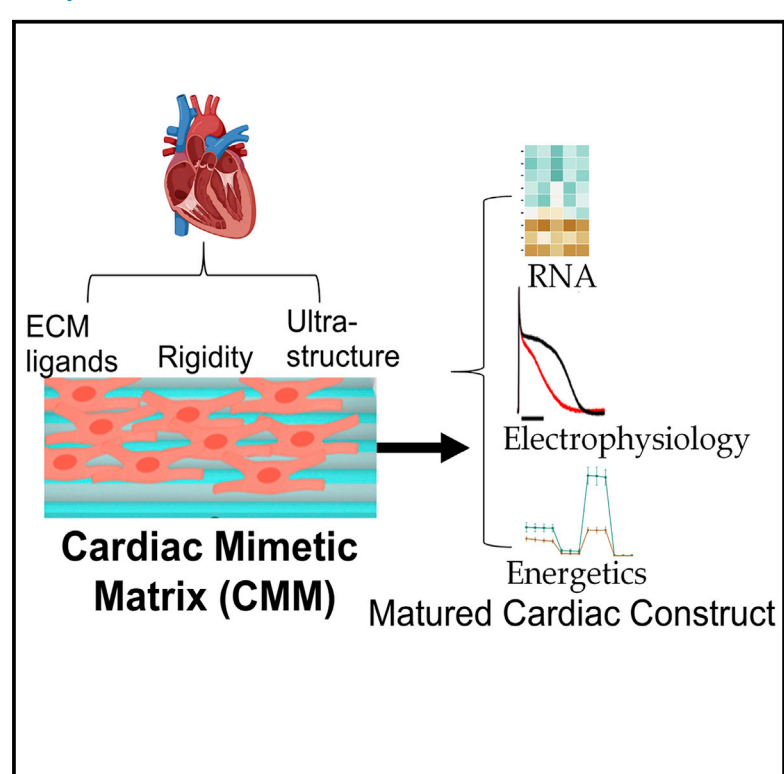
Cardiac ultrastructure inspired matrix induces advanced metabolic and functional maturation of differentiated human cardiomyocytes

Graphical abstract



Authors

Junaid Afzal, Yamin Liu, Wenqiang Du, ..., Alix C. Deymier, Lixia Yue, Kshitiz

Correspondence

junaid.afzal@ucsf.edu (J.A.), kshitiz@uchc.edu (K.)

In brief

Afzal et al. induce physiologically inspired cardiac maturation. The resulting cardiac constructs display features of ventricular myocytes within 30 days including structural alignment, electrophysiological maturation, molecular signature, mitochondrial energetics and fatty acid oxidation, and efficient oxidative stress handling capability, facilitating their use in disease modeling and preclinical drug screening.

Highlights

- Rapid iPSC-CM maturation on surfaces mimicking native cardiac microenvironment
- Concurrent metabolic and redox maturation on cardiac mimetic matrix (CMM)
- Hybrid Steiner tree network identifies intermediaries involved in cardiac maturation
- Cardiac ultrastructure moderates hypertrophic disease phenotype







Article

Cardiac ultrastructure inspired matrix induces advanced metabolic and functional maturation of differentiated human cardiomyocytes

Junaid Afzal,^{1,*} Yamin Liu,^{2,9} Wenqiang Du,^{2,9} Yasir Suhail,^{2,3,9} Pengyu Zong,^{4,5} Jianlin Feng,^{4,5} Visar Ajeti,^{2,3} Wasim A. Sayyad,⁶ Joerg Nikolaus,⁷ Maya Yankova,⁸ Alix C. Deymier,² Lixia Yue,^{4,5} and Kshitiz^{2,3,4,10,*}

https://doi.org/10.1016/j.celrep.2022.111146

SUMMARY

The vast potential of human induced pluripotent stem-cell-derived cardiomyocytes (hiPSC-CMs) in preclinical models of cardiac pathologies, precision medicine, and drug screening remains to be fully realized because hiPSC-CMs are immature without adult-like characteristics. Here, we present a method to accelerate hiPSC-CM maturation on a substrate, cardiac mimetic matrix (CMM), mimicking adult human heart matrix ligand chemistry, rigidity, and submicron ultrastructure, which synergistically mature hiPSC-CMs rapidly within 30 days. hiPSC-CMs matured on CMM exhibit systemic transcriptomic maturation toward an adult heart state, are aligned with high strain energy, metabolically rely on oxidative phosphorylation and fatty acid oxidation, and display enhanced redox handling capability, efficient calcium handling, and electrophysiological features of ventricular myocytes. Endothelin-1-induced pathological hypertrophy is mitigated on CMM, highlighting the role of a native cardiac microenvironment in withstanding hypertrophy progression. CMM is a convenient model for accelerated development of ventricular myocytes manifesting highly specialized cardiac-specific functions.

INTRODUCTION

As robust protocols were developed to differentiate human induced pluripotent stem cells (hiPSCs) into beating cardiomyocytes (hiPSC-CMs), expectations were built up to create human adult-like cardiac tissue constructs for applications in regenerative medicine, toxicity screens, and precision medicine. However, hiPSC-CMs exhibit immature phenotypes reminiscent of very early stages of heart development with limited applicability (Karakikes et al., 2015). This is not surprising, considering that typically differentiation is carried on an aphysiological matrix and is shorter than in utero cardiac development (Goversen et al., 2018). This observation has motivated several efforts to increase maturation of hiPSC-CMs by presenting microenvironmental factors present in the developing heart (Feaster et al., 2015; Jung et al., 2015; Kaiser et al., 2019), or transplanting directly into small animal hearts (Cho et al., 2017; Passier et al., 2016). These stimuli include electrical stimulation, nanotopographic substrates, hormones, metabolic

or mechanical preconditioning, and engineered heart tissues (Hu et al., 2018; Khan et al., 2015; Ronaldson-Bouchard et al., 2018; Ruan et al., 2016; Shadrin et al., 2017; Wrighton et al., 2014). While engineered heart tissues and other threedimensional (3D) methods show structural and electrophysiological maturation, sophisticated studies on signaling dynamics, metabolism, and mitochondrial energetics necessitate more reductive two-dimensional (2D) systems, with additional advantage of increased reproducibility and scalability and reduced resource intensiveness. Adult cardiomyocytes are highly specialized in generating sufficient and repeated forces for long durations. This functional requirement necessitates a specialized ultrastructure and metabolism, with a large number of mature mitochondria, dependence on oxidative phosphorylation (OxPhos) and fatty acid oxidation (FAO), and energy substrate plasticity (Bers, 2002; Hom et al., 2011; Stanley et al., 2005; Yang et al., 2014). However, metabolic maturation has not been convincingly demonstrated in current cardiac constructs.



¹Department of Medicine, Division of Cardiology, University of California, San Francisco, San Francisco, CA 94158, USA

²Department of Biomedical Engineering, University of Connecticut Health, Farmington, CT 06032, USA

³Center for Cellular Analysis and Modeling, University of Connecticut Health, Farmington, CT 06032, USA

⁴Department of Cell Biology, University of Connecticut Health, Farmington, CT 06032, USA

⁵Calhoun Cardiology Center, University of Connecticut Health, Farmington, CT 06032, USA

⁶Department of Cell Biology, Yale University, New Haven, CT 06510, USA

⁷West Campus Imaging Core, Yale University, New Haven, CT 06477, USA

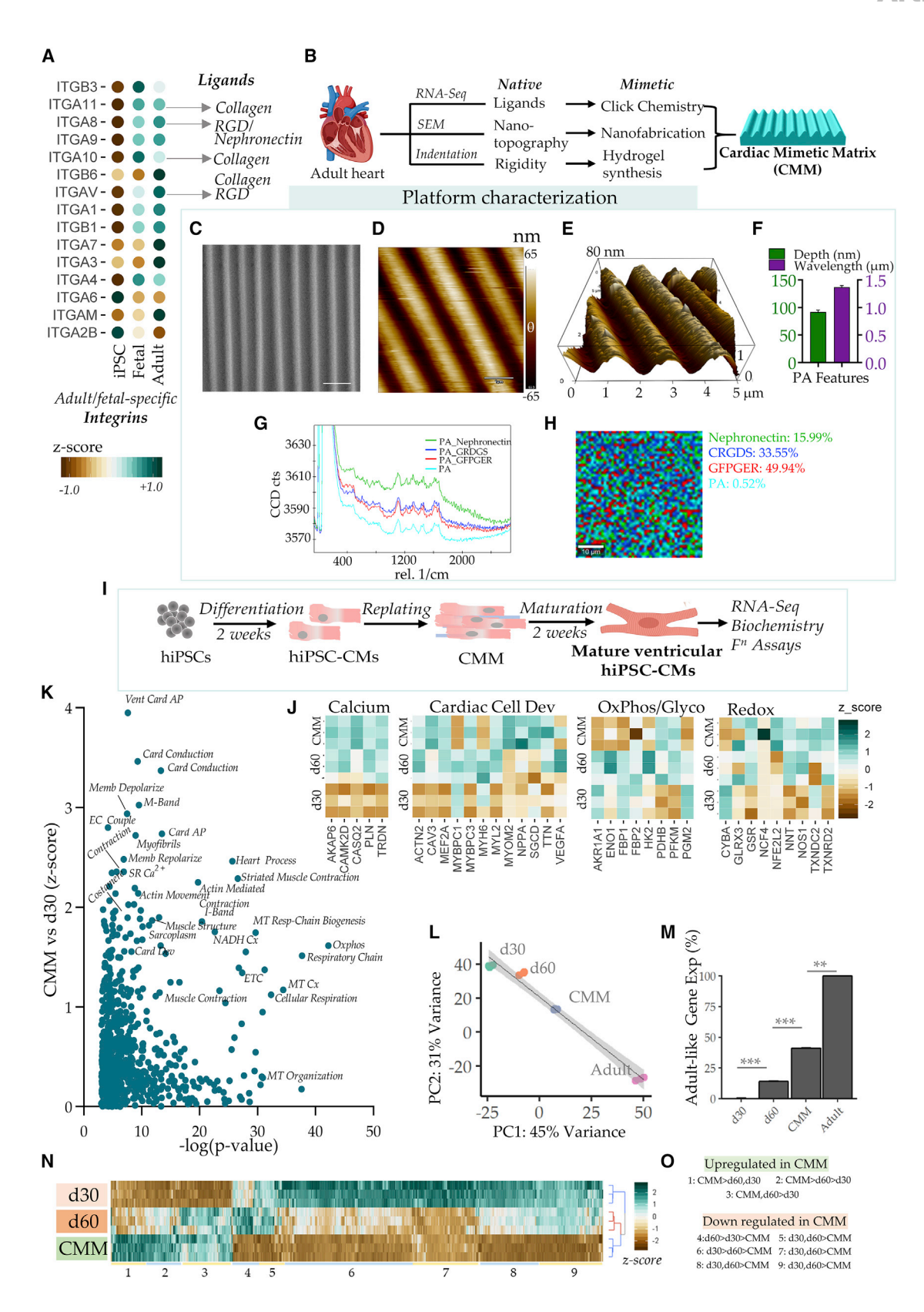
⁸Electron Microscopy Core, University of Connecticut Health, Farmington, CT 06032, USA

⁹These authors contributed equally

¹⁰Lead contact

^{*}Correspondence: junaid.afzal@ucsf.edu (J.A.), kshitiz@uchc.edu (K.)





(legend on next page)

Article



A substantial body of literature indicates that the matrix microenvironment is crucial to the specification, development, and maintenance of tissue-specific parenchyma (Ayad et al., 2019; Mammoto and Ingber, 2010; Vining and Mooney, 2017). We presented the matrix ligands inferred via integrin subtypes present in the adult heart and combined it with the mechanical and ultrastructural milieu mimicking the heart matrix consisting of anisotropic nanowrinkled hydrogel with the elasticity of heart matrix, together termed the cardiac mimetic matrix (CMM). We found that presentation of these factors, in combination, synergistically accelerated maturation of differentiated hiPSC-CMs.

Using RNA sequencing and a combination of structural and functional readouts, we found that CMM significantly enhanced maturation of cultured hiPSC-CMs toward the adult human heart state within 30 days, faster than in comparison with well-differentiated cells in regular culture conditions. CMM induced systemic programming of cardiac development-related transcription and more aligned sarcomeric organization, increased mechanical force generation, and improved calcium handling. Patchclamp-based and optical probes-based electrophysiological measurement showed development of mature ventricular cardiomyocytes, with core cardiac ion channel pharmacological sensitivity.

We observed hiPSC-CMs matured on CMM to rely primarily on OxPhos and FAO (Lopaschuk and Jaswal, 2010), as well as having highly fused and abundant mitochondria. hiPSC-CMs on CMM also exhibited high redox scavenging capability, required by adult cardiomyocytes reliant on oxidative phosphorylation (Burgoyne et al., 2012; Santos et al., 2011). Assessment of early hypertrophic response on CMM highlighted the ameliorative role of cardiac ultrastructure to withstand disease progression. In conclusion, we present CMM as a method to create structurally anisotropic and electromechanically coupled cardiac constructs, which are metabolically, mechanically, and structurally closer to an adult human heart than prolonged cultures in a convenient 2D platform, enabling scaled interrogations for disease modeling, drug screening, and regeneration, or as models of the developing heart.

RESULTS

Cardiac mimetic matrix synergistically promotes maturation of cardiomyocytes

We hypothesized that maintaining differentiated hiPSC-CMs with physiological factors present in the developed heart tissue may support their maturation (Schwach and Passier, 2019). We sought to create a substratum matching the chemistry, elasticity, and topographic ultrastructure of the extracellular matrix (ECM) to which that adult cardiomyocytes respond. Integrin α and β subunits combine to form more than 20 different heterodimers with varying ligand specificity and transduce extracellular chemical and mechanical information to intracellular signaling modulating various cellular phenotypes, including cell fate and differentiation (Kshitiz et al., 2012; Mamidi et al., 2018). We used adult human hearts transcriptomic data (Choy et al., 2015; He et al., 2016; Lopez-Acosta et al., 2018; Zhao et al., 2019) and identified genes encoding integrin receptor subunits upregulated in comparison with hiPSCs (Figure 1A). Adult human cardiomyocytes expressed higher levels of transcripts encoding integrins specific for widely used matrix peptide motifs, including RGD and collagen-binding $\alpha 11$, $\alpha 10$, and $\alpha 1$ subunits. $\alpha 7$ and $\alpha 3$, receptors for laminin, were also highly expressed in adult heart, although α6 expression was low (Burridge et al., 2014; Sung et al., 2020). In addition, a8 was also upregulated with high specificity for nephronectin, responsible for cardiac development and cardiomyocyte adhesion (Patra et al., 2011, 2012) (Figure 1A).

We and others have previously shown that nanoarchitectured substrates mimicking the ultrastructure of the heart matrix increase tissue organization and structural maturation of cultured cardiomyocytes (Carson et al., 2016; Crowder et al., 2013; Kim et al., 2012; Kshitiz et al., 2014; Liu et al., 2015; Smith et al., 2017). In addition, it is well recognized that substratum mechanics fundamentally influences cell differentiation (Ayad et al., 2019; Mammoto and Ingber, 2010). We therefore surmised that combining nanoarchitectured substrates, elasticity matching heart tissue, and adult-cardiomyocyte-inspired ligand chemistry may, in combination, affect hiPSC-CM maturation. Based on transcriptomic analysis of integrins present in the adult human heart, we conjugated RGD, GFOGER (a commercial alternative to GFOGR), and nephronectin in equal amounts with hydrogel patterns into nanoarchitectured arrays produced by anisotropic nanowrinkle pattern transfer to create a CMM substrate (Figure 1B). We created a nanowrinkled polydimethylsiloxane (PDMS) substrate, which recapitulates cardiac matrix ultrastructure more than completely anisotropic arrays (Caulfield and Janicki, 1997; Silva et al., 2020), transferred the pattern to polyurethane molds, and thereafter into polyacrylamide (PA) hydrogels matching heart matrix elasticity. A double transfer was necessitated because PA required a mold non-permeable to atmospheric oxygen. Scanning electron microscopy (SEM)

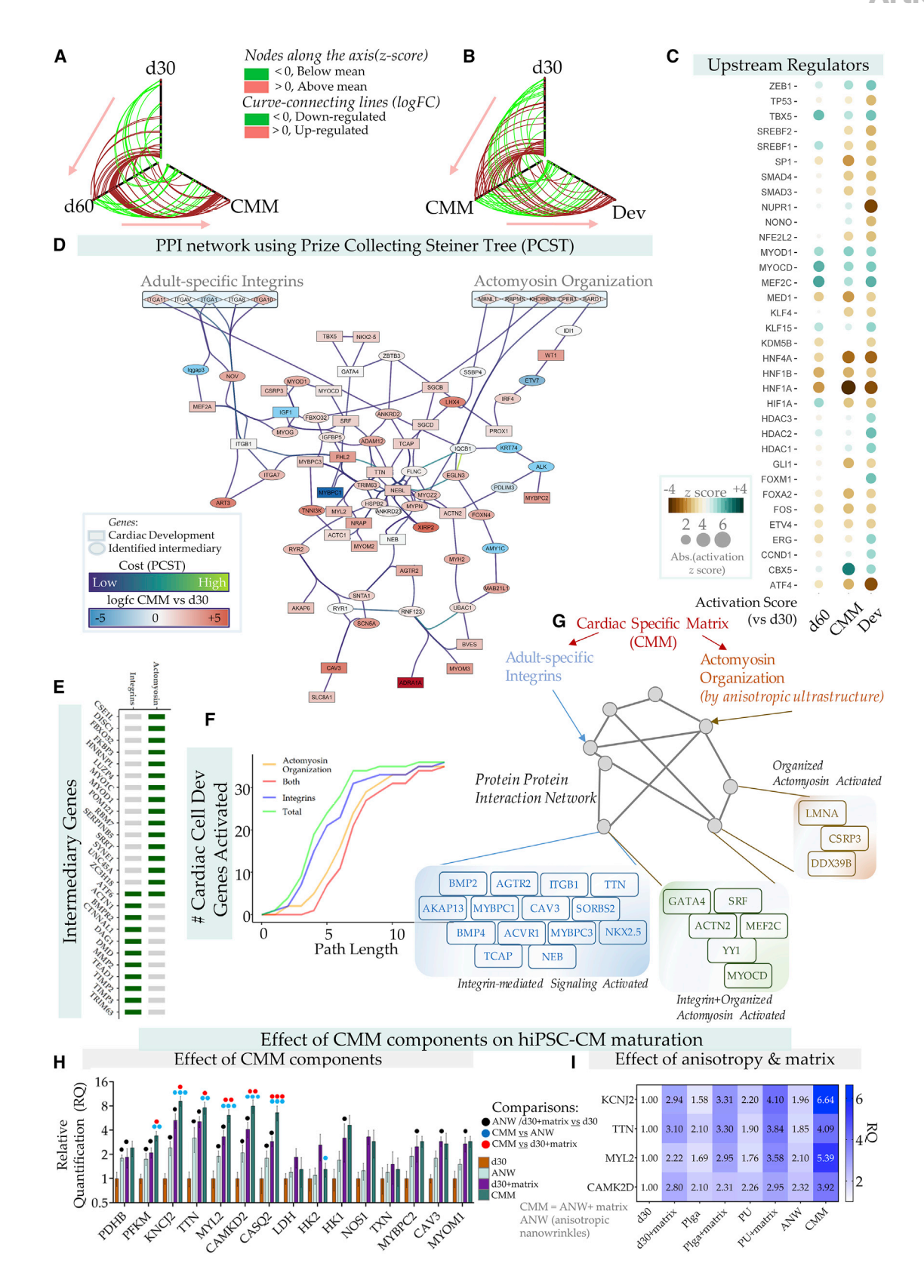
Figure 1. Adult heart-like matrix ligands, elasticity, and ultrastructure drive a systemic maturation of differentiated human cardiomyocytes (A) Expression of integrin genes in adult and fetal hearts versus iPSCs.

⁽B) Selected ligands were conjugated to a substrate with anisotropic nanowrinkles (ANW) with Young's modulus of 23 kPa to form cardiac mimetic matrix (CMM). (C-F) (C) SEM image of polyurethane substrate with ANW. Scale bar, 2.5 μm. (D) AFM image of CMM. Scale bar, 1 μm. (E and F) Rendering of CMM topographical features and their quantification; n > 6 features.

⁽G and H) (G) Raman spectroscopy of conjugated peptides on PA hydrogel. (H) Raman spectroscopic xy scan showing bound ligands on CMM. Scale bar, 10 µm. (I) Schematic showing study design.

⁽J-O) RNA sequencing-based analysis. (J) Genes in key functional categories related to cardiac maturation. (K-M) Unbiased differential gene set analysis between CMM and after 30 days (d30). Cx, complex; AP, action potential; ETC, electron transport chain; MT, mitochondria; SR, sarcoplasmic reticulum. (L and M) CMM accelerates cardiac development and maturation. (L) Maturation path of hiPSC-CMs toward adult heart captured in a linear path within the two largest PCs obtained from transcriptomic states of 30 days of culture (d30 and CMM), d60, and adult heart; blue line denotes the best fit curve, gray band denotes 95% confidence interval. (M) Adult-like gene expression obtained from cardiac maturation vector, p < 0.01 (**) or p < 0.001 (***). (N and O) (N) Hierarchical clustering of gene expression. (O) Cluster identity and relative expression of d30, d60, and CMM samples.





(legend on next page)

Article



(Figures 1C, S1A, and S1B) and atomic force microscopy (AFM) (Figures 1D-1F and S1C) showed that nanowrinkled PDMS patterns transferred to polyurethane acrylate (PUA) (Figure 1C) and thereafter to the hydrogel (Figures 1D-1F) were anisotropic, similar to the aligned bundles of collagen fibers in the heart (Figures 1F and S1D) (Kshitiz et al., 2014) with matching substrate elasticity (Kshitiz et al., 2012). Raman spectroscopic confocal microscopy confirmed a spatially uniform and equal distribution of RGD, GFOGR, and nephronectin conjugation (Figures 1G and 1H). We then tested the capability of CMM to mature differentiated hiPSC-CMs. hiPSCs were differentiated into beating cardiomyocytes using a well-established protocol (Burridge et al., 2014) and metabolically purified using lactate yielding >95% TNNT2+ cells (Figures S1E and S1F) (Burridge et al., 2014; Tohyama et al., 2013) of high quality, comparable with multiple studies (Figures S2A-S2C). Cells were plated on tissue-culture plastic with fibronectin as control for a total of 30 days (d30), for prolonged culture of 60 days as positive control (d60), or on CMM surfaces on days 13-14 until day 30 (Figure 11). After termination of the experiment, RNA was collected, sequenced, and analyzed, and functional tests performed. We found that culture on CMM resulted in significant and substantial upregulation of important genes related to key characteristics of ventricular cardiomyocytes, including calcium handling (CAMK2D, CASQ2, PLN, TRDN), cardiac development (MYOM2, TTN, MYBPC3, CAV3), and cardiac-type metabolism (PFKM, PDHB, NEFL2, NNT, NOS1, GSR) (Figures 1J and S3).

CMM accelerates systemic gene transcription toward an adult-like state

Considering the short period of culture on CMM, we found many gene sets to be different in CMM versus d30 (p < 0.05), surprisingly most being related to cardiac function (Figure 1K). CMM resulted in upregulation of several key ontologies related to cardiac electrophysiological development (ventricular cardiac action potential [AP], cardiac conduction, sarcoplasmic reticulum [SR] calcium), structural maturation (muscle structure, muscle contraction), and metabolic processes (OxPhos, cellular respiration, NADH complex, mitochondrial respiratory chain biogenesis, and organization) (Figure 1K). We compared global transcription in cells cultured on CMM and on control substrate for 30 and 60 days with published data of adult human heart samples (Choy et al., 2015; Dias et al., 2018; He et al., 2016; Lewandowski et al., 2018). Principal component analysis of the two largest components (accounting for 75% of variance) showed a strong linear regression suggesting a systemic movement of cellular transcription toward a more adult-like state (Figure 1L). This regression could be construed as a cardiac maturation vector, with cells cultured on CMM being more adult-like than d30, as well as ahead of d60 (Figure 1M). Hierarchical clustering on Z-normalized data showed enrichment of gene sets in CMM (cluster 1) related to cardiac muscle maturation, ECM binding, collagen synthesis, assembly, crosslinking, and organization (Figures 1N and S4A-S4C; Table S1), indicating that hiPSC-CMs were highly receptive to physiological matrix as well as gene sets related to mature actomyosin assembly, striation, and increased contractility (cluster 2). Other gene sets were also directed toward a trend of increased cardiac maturation on CMM (Figures S4A and S4B).

CMM accelerates the transcriptional program for cardiac development

Tracing individual gene expression change along the stages of maturation, d30 to d60 to CMM to fetal to adult (Figure S5A), confirmed the general trend of a transcriptomic cardiac maturation vector (Figures 1L and 1M). Hive plots for cardiac development ontology showed that CMM resulted in accelerated upregulation of many genes within 30 days, similar to prolonged culture for 60 days (Figures 2A and 2B). Upstream regulators predicted by Ingenuity pathway analysis (IPA) contained many transcriptional factors (TFs) related to cardiac development activated in CMM, as well as in developed heart, many activated in CMM even more than in the prolonged d60 condition (Figure 2C). These TFs included many SMADs, cardiac-specific TFs MYOD1, MYOCD, MEF2C, and TBX5. The global persistence of genes suggested activation of a cardiac development-related transcriptional program that strengthens as cells change their state along the cardiac maturation vector.

CMM induces cardiac maturation by synergistic combination of cardiac-specific matrix ligands, ultrastructure, and mechanics

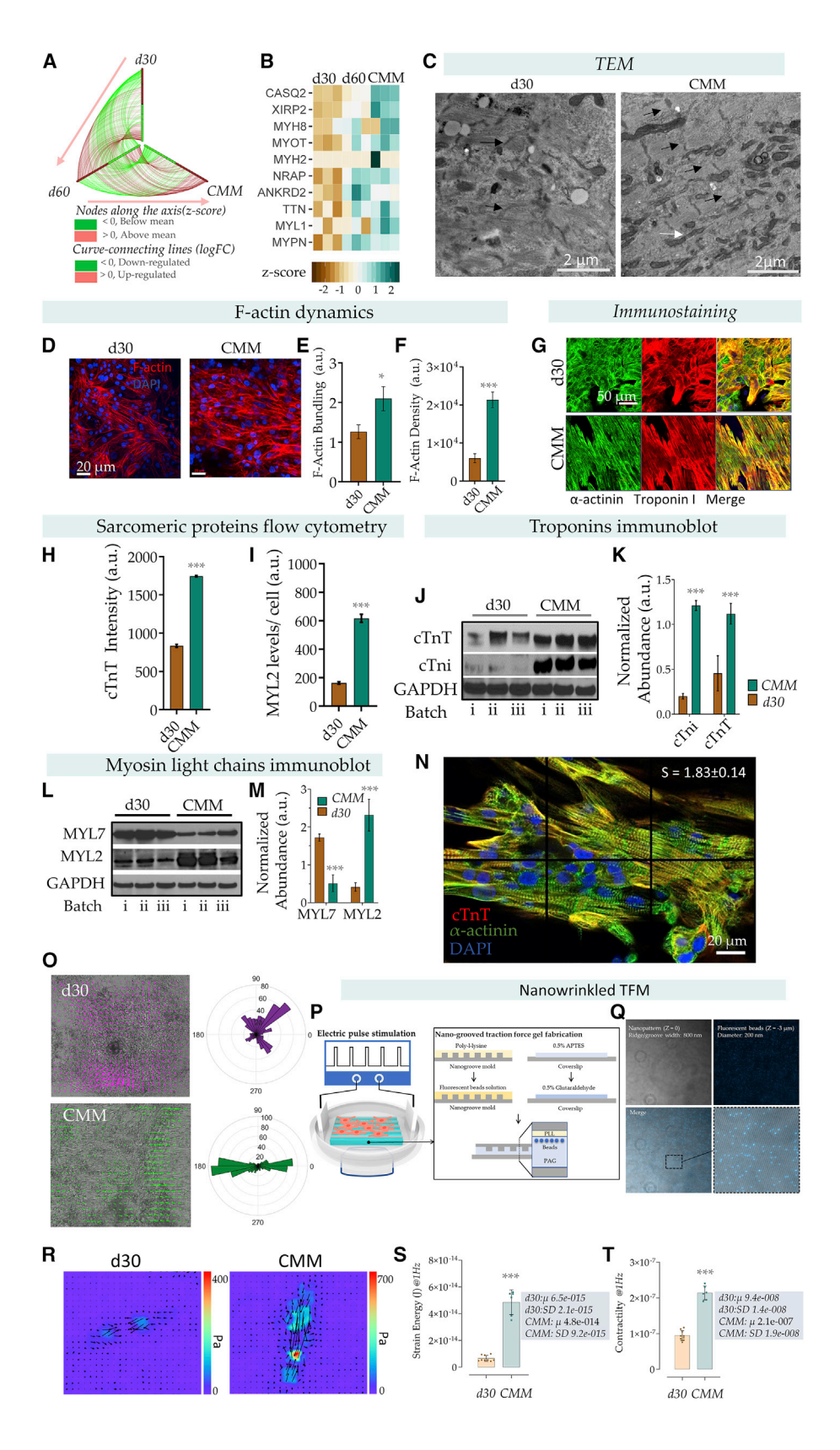
CMM is a composite platform consisting of specific ligand chemistry, matrix mechanics, and ultrastructure. To assess their relative contribution and identify potential signaling intermediaries involved, we created a networking analysis method using the Prize Collecting Steiner Tree formulation (see STAR Methods) (Akhmedov et al., 2017; Bienstock et al., 1993). The resultant subnetwork connects CMM constituents (ligand chemistry and mechanics) with the genes related to cardiac development

Figure 2. CMM transcriptionally upregulates cardiac development

(A and B) Hive plots showing changes in gene expression of cardiac development genes between (A) d30, d60, and CMM; and (B) d30, CMM, and developed (Dev)

- (C) Activation scores of transcription factors (TFs) between d60, CMM, and Dev in comparison with d30 culture.
- (D-F) A subnetwork of protein-protein interactions relating input: (i) integrins targeted in CMM, and (ii) top expressed genes in actomyosin organization ontology to target: cardiac development genes. For details see STAR Methods. Predicted intermediary genes are in ovals; colors indicate CMM versus d30 expression, and are listed for a path length of 5 (from inputs to target) in (E).
- (F) The number of target genes activated or reached from either input against the maximal lengths of paths through the network.
- (G) The set of targets, i.e., cardiac development genes activated by the integrins and actomyosin organization genes with path lengths of 5 or less in the network constructed from multivalidated PPIs.
- (H) Relative quantification using RT-PCR of key genes associated with cardiac maturation. For details of individual components in CMM, see STAR Methods.
- (I) Heatmap with relative quantification (RQ) of select cardiac transcript expression using RT-PCR on different substrates (with and without matrix). Statistical comparison done by One-way ANOVA with post-hoc Tukey test; p < 0.05(.), p < 0.01(..), p < 0.001(...).





Article



through BioGRID interactome (Stark et al., 2006). We used genes in actomyosin organization ontology as a surrogate for those influenced by anisotropic matrix and physiological elasticity, while adult-heart-specific integrins were used as the second input into the protein-protein interaction (PPI) network, prioritizing inclusion of genes differentially upregulated in CMM versus control. We generated a comprehensive network connecting the five integrin genes in adult heart and the top five genes (Figure 2D), or weighted input of the whole actomyosin organization ontology (Figure S5B). Both networks succinctly captured candidate intermediaries also mostly upregulated in CMM (Figures 2D and S5B), including TNNI3, MYOD1, MYPN, MYH2, XIRP2, RYR1, and RYR2 (Friedman et al., 2018; Paige et al., 2015; Thompson et al., 1991; Uosaki et al., 2015) (Figures 2D and S5B). Within a path length of 5, we surprisingly found nearly exclusive subnetworks suggesting an additive effect of both inputs, with ATF6 as the common intermediary (Figure 2E). With more gene inputs, we found a few more non-exclusive intermediaries (ACTN1, DAG1, NBR1, and TRIM63), but subnetworks remained largely mutually exclusive (Figure S5C). Counting the number of gene targets reached for a given path length, we found either input synergistically reaching multiple target nodes in relatively short paths (Figures 2F and S5D), chiefly ACTN2, CAV3, GSK3A, MYBPC1/3, GATA4, MEF2C, MYOCD, and SRF (Figures 2G and S5E).

We then experimentally tested the prediction of synergistic effect of individual components of CMM for cardiac transcripts and mitochondrial maturation. Cells were plated on flat (d30), matrix conjugated (d30 + matrix), anisotropic nanowrinkled (ANW) surfaces, and ANW surfaces conjugated with matrix (CMM) (Figure 2H). RT-PCR analysis on a panel of key cardiacspecific genes showed that ligands and ultrastructure had a synergistic effect on CMM (Figure 2H). Culture on CMM showed increase in key metabolic, structural, and calcium/electrophysiological genes, including PDHB, PFKM, KCNJ2, TTN, MYL2, CAMK2D, and CASQ2. We also tested the effect of alternative nanotextured substrates combined with cardiac-specific matrix ligands. RT-PCR of key markers for cardiac maturation showed that CMM induced superior maturation compared with aligned electrospun poly(lactide-co-glycolide) (PLGA), and aligned capillary force lithography (CFL)-based PUA substrates (Figures 2I, S6A, and S6B) (Carson et al., 2016; Choi et al., 2020; Kumar et al., 2020; Yu et al., 2014). Mitochondrial DNA quantification confirmed a similar trend on CMM versus anisotropic PLGA electrospun fibers and CFL substrates (Figure S6B). RT-PCR and mitochondrial DNA also demonstrated maturation of cardiomyocytes derived from other iPSC cell lines on CMM (Figures S7A and S7B). Together with the PPI subnetwork analysis, these data showed that mechanochemical cues in CMM synergistically influenced cardiac development. We then sought to characterize the cardiac-specific phenotypes of CMM matured cardiac constructs, positioning their structure, metabolism, and function contextually to the adult-like hallmarks of cardiac behavior (Yang et al., 2014).

Differentiated cardiomyocytes are structurally mature on CMM

We first characterized whether CMM-induced changes in gene expression resulted in accompanying maturation in the structural and mechanical characteristics. Focusing on ontologies related to cardiac structure, we found that CMM caused an increase in gene expression even more than d60 (Figure 3A). Top genes with correlated increase on CMM and developed heart showed higher expression on CMM compared with d30 and even d60 (Figure 3B). Transmission electron microscopy (TEM) showed that cells on CMM contained structurally organized and aligned arrangement of multiple sarcomeres bundled parallel to each other, and many enlarged and elongated mitochondria (Figures 3C, S8A, and S8B). Confocal microscopy revealed highly bundled and directionally aligned F-actin strands (Figures 3D-3F and S9A), with higher z-axis depth, indicating more voluminous microfilamentous architecture on CMM versus d30 (Figure S9A). Immunostaining for α -actinin and troponin I showed aligned myofibrils in cells on CMM versus d30 (Figure 3G), Cardiac troponins form key structural components of muscle cell sarcomeric architecture and determine the maturation of iPSC-CMs (Bedada et al., 2016). RT-PCR showed significant upregulation of cardiac troponin

Figure 3. CMM promotes structural maturation of differentiated cardiomyocytes

(A and B) CMM increases expression of genes associated with structural maturation of cardiomyocytes. (A) Hive plot showing relative expression of genes associated with structure-related pathways (regulation of actin cytoskeleton, focal adhesion, ECM receptor interaction, and gap junctions). (B) Top ten cardiac structure-related genes upregulated in CMM versus d30.

(C) Ultrastructure analysis using TEM shows aligned sarcomeric structures on CMM compared with d30. Black arrows perpendicular to myofibril Z band, white arrows: mitochondria. Z bands are oriented in same direction on CMM.

(D–F) Aligned and thick F-actin fibers on CMM; n > 4 samples.

(G) Two-photon images of troponin I and α-actinin indicate aligned sarcomere on CMM compared with disoriented sarcomere in d30.

(H and I) Flow-cytometry analysis of sarcomeric proteins Myl2 (H) and cTnT (I).

(J-M) Higher abundance of cardiac troponins (TnT, TnI) (J and K) and myosin light chain 2 isoforms (L and M) on CMM versus d30. Immunoblot is presented as + SD with three biological replicates, p < 0.001(...).

(N) Airyscan image of cells on CMM stained with cardiac troponin T and α-actinin shows banding. Sarcomere length (inlet): 1.83 ± 0.14 μm. Data are presented as ±SD.

(O) Overlay of velocity vectors (length: contractile magnitude; angle: direction of contraction) determined by particle image velocimetry on phase-contrasted monolayers of hiPSC-CMs on CMM (green) or control (purple) during spontaneous contraction.

(P and Q) Anisotropic nanowrinkle (ANW)-incorporated traction force microscopy (TFM). (P) Schematic showing electric pace stimulation of hiPSC-CMs on ANW-TFM substrate. (Q) Images showing embedding of fluorescent beads \sim 3 μ m below nanowrinkled pattern.

(R) TFM strain energy density maps for d30 and CMM.

(S and T) Strain energy and contractility levels of cells for CMM and d30 at 1 Hz paced cells; significance was calculated using one-way Anova with Tukey's correction, p < 0.001(...).



isoform (Tnni3) and downregulation of slow skeletal isoform of Tnni1 on CMM (Figure S9B). Flow-cytometry distribution of cardiac troponin T (cTnT) showed higher cTnT levels per cell (Figures 3H and S9C), as well as enrichment of a cTnThigh subpopulation (all cells were cTnT+ve) (Figure S9C), a trend observed for another key sarcomeric component, myosin light chain-2 (Figures 3I and S9D). Immunoblotting confirmed significantly higher levels of cTnT and cardiac troponin I (cTnI) on CMM versus d30 (Figures 3J and 3K). As cardiomyocytes mature, relative abundance of isoform for myosin light chain MYL2 increases versus MYL7, a useful marker for a more developed state (Guo and Pu, 2020). Immunoblotting showed a clear increase in relative abundance of MYL2 versus MYL7 isoforms in CMM versus control (Figures 3L and 3M). Confocal imaging for MYL2 with α-actinin showed non-overlapping abundance on sarcomeres, with well-separated bands (~1.8 μm) observed on CMM (Figures S9E-S9H) (Lundy et al., 2013). Furthermore, Airyscan imaging showed extensive overlapping strands stained for wheat germ agglutinin (WGA) (Figure S10A; Video S1 shows 3D arrangement of lectin). Connexin-43-stained gap junctions also showed the classic punctate structures between cells, as well as organized series of intercellular junctions (Figure S10B). Airyscan also showed cTnT and α-actinin distributed in adjacent locales within the sarcomeres with staggered expression patterns, indicating a high degree of sarcomeric maturation/myofibrillar bundles in cells on CMM (Figures 3N and S10C-S10E; Video S2). Airyscan also confirmed the sarcomere length to be $\sim\!1.83\pm0.14~\mu m$ on matured cardiomyocytes on CMM (Figure S10C).

CMM enhances mechanical maturation and force generation capability of differentiated cardiomyocytes

Cardiomyocytes are contractile cells capable of force generation upon electrical stimulation. Increased structural maturation and high mitochondrial content in hiPSC-CMs on CMM suggested increased capability to produce contractile force. Particle image velocimetry on time-lapsed images of cells revealed contraction velocity vectors being randomly aligned on control substrate while being more sustained and highly directional on CMM (Figure 3O). Duration of beats on CMM was twice as long as on d30, while spontaneous beating was significantly reduced (Figures 3O, S10F, and S10G). To directly quantify the force-generating capacity of cells, we augmented traction force microscopy (TFM) on anisotropic nanowrinkled substrates by embedding fluorescent beads below the nanowrinkles (Figures 3P, 3Q, and S10H) (Knoll et al., 2014). TFM measures traction forces applied by a cell to the substratum via integrins tethered to the matrix and the force-generating actomyosin assembly within. However, because cells are unloaded, the direct relation between traction force and contractile force may break down under very high pacing rates. TFM offers advantages beyond its subcellular resolution, as it can be combined with many microscopy-compatible probes to elicit a direct relationship between force generation and cell signaling or metabolic activity. We placed nano-TFM with cultured cells in a pacing chamber, measuring their contractility and strain energy upon external pacing compared with d30. hiPSC-CMs on CMM had a many-fold increase in strain energy

(Figures 3R, 3S, and S10K) and directional contractile force generation (Figures 3T and S10L). High temporal resolution imaging confirmed mechanical contraction coupled to pacing (Figure S10J). Overall, the data showed increased structural maturation on CMM accompanied by markedly higher forcegenerating capability.

CMM exhibits hallmarks of adult-like metabolism

Cardiac tissue is highly metabolically active and dependent on mitochondrial oxidative respiration (Lopaschuk and Jaswal, 2010), with a high plasticity in substrate utilization, essential for rapidly generating ATP, which is limiting; ~10 mM lasting for a few contractions (Ingwall, 2009; Stanley et al., 2005). Transcriptomic data indicated that hiPSC-CMs on CMM follow a more adult cardiac metabolic program, with increased expression of key transcripts in electron transport chain (ETC), FAO, and OxPhos (Figures 4A and S4). To evaluate the metabolic signature of cells on CMM, we performed a comprehensive investigation of energetics to characterize cellular and mitochondrial metabolism in both intact cells (for OxPhos and glycolysis) and permeabilized cells (for ETC activity and FAO). We found that cells on CMM demonstrate significantly higher oxygen consumption rate (OCR) in comparison with the d30 (Figure 4B). Compared with d30, cells on CMM exhibited higher OCR in intact cells at baseline from 81 pmol/min to 151 pmol/ min, coupled respiration (oligomycin-sensitive respiration) from 65 pmol/min to 141 pmol/min, and uncoupling capacity (carbonyl cyanide-p-trifluoromethoxyphenylhydrazone [FCCP]) from 140 pmol/min to 425 pmol/min, indicating significantly higher OxPhos capacity (Figure 4B). We did not observe significant differences in basal glycolysis levels (extracellular acidification rate [ECAR]) in cells on CMM versus d30 (Figure 4C). We then investigated the maturation of mitochondrial energetics by measuring complexes I and II of ETC and FAO in permeabilized cells (Figures 4D and 4E). Activity of complex I/II of ETC was measured at basal rates/state 4 (substrate only) using 5 mM glutamate/malate and 5 mM succinate, respectively, and active/state-3 respiration was measured with the addition of 4 mM ADP. We observed increases in both state-4 and state-3 ETC activity in cells cultured on CMM, indicating higher mitochondrial ETC activity (Figure 4D). Using 200 mM palmitoyl-CoA carnitine, we observed increased FAO in cells on CMM versus control (Figure 4E). The 2D nature of CMM facilitated measurement on permeabilized cells, necessary to directly measure ETC chain activity and substrate utilization.

Dependence on OxPhos and a high rate of ATP generation result in a high burden of reactive oxygen species (ROS), which adult-like cardiac cells can scavenge by maintaining 100-fold higher reduced glutathione (GSH) than the oxidized species (oxidized GSH [GSSG] and mixed disulfide [GSSR]) (Burgoyne et al., 2012; Santos et al., 2011) (Aquilano et al., 2014). Using a pulse of 1 mM hydrogen peroxide (H₂O₂) in Tyrode buffer, we evaluated the recovery of oxidized glutathione pool of hiPSC-CMs using a cytoplasmic Grx1-roGFP2 probe (Gutscher et al., 2008; Meyer and Dick, 2010). Grx1-roGFP2 signal intensity was normalized by respective addition of diamide and dithiothreitol (DTT) for maximum and minimum signal (Meyer and Dick, 2010). We found a stable Grx1-roGFP2 signal





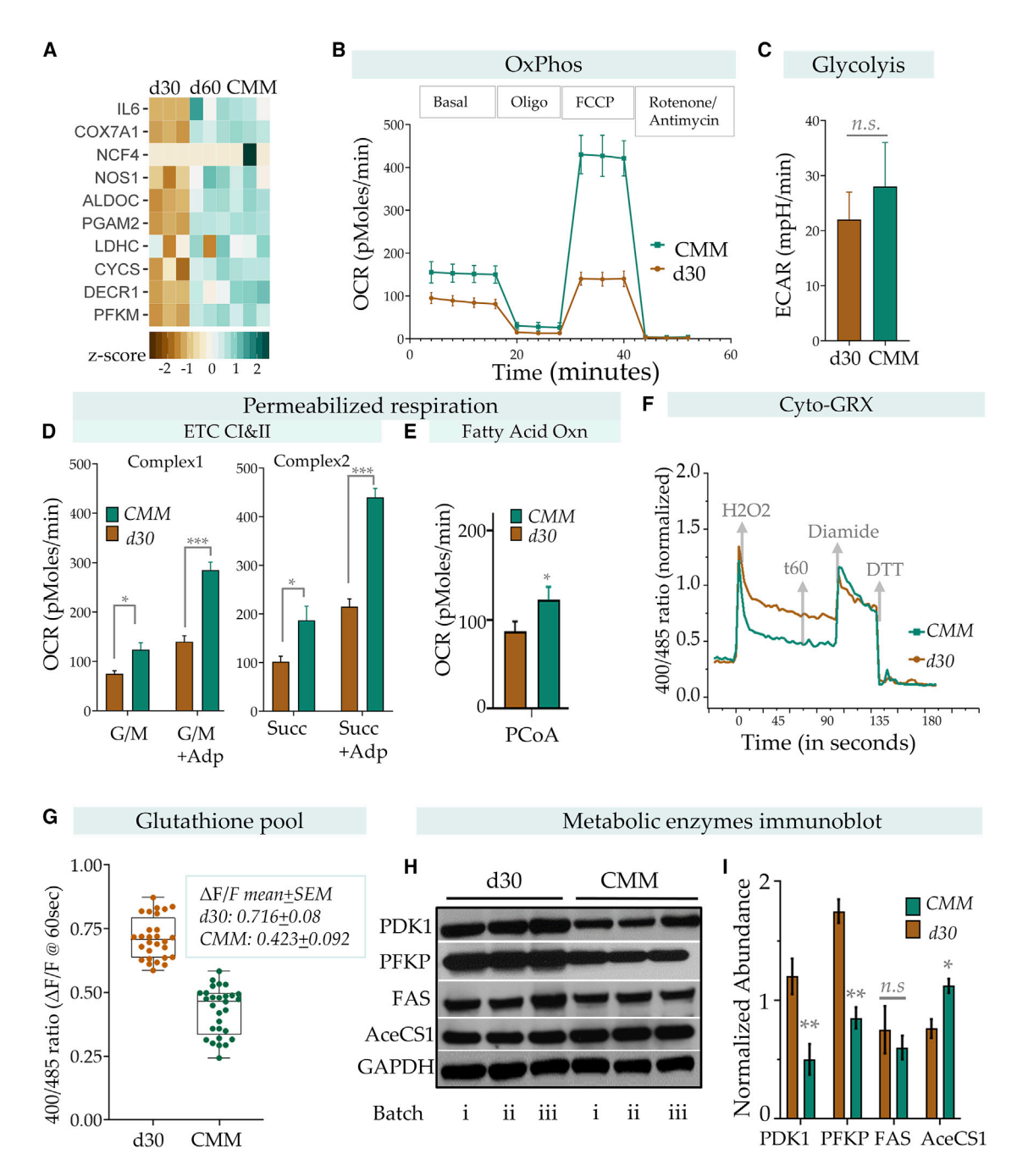


Figure 4. Metabolic maturation of cardiomyocytes is accelerated by CMM

(A) Heatmap of top ten genes upregulated in CMM versus d30.

(B-E) CMM increases respiration of hiPSC-CMs. In intact cells, (B) hiPSC-CMs cultured on CMM showed increase in basal, coupled (oligomycin-sensitive), and uncoupled (FCCP-sensitive) respiration, but not in glycolysis (C).

(D and E) Permeabilized respiration. (D) State-4 and state-3 respiration for CMM versus d30. (E) oxidation of long-chain fatty acid (200 µM palmitoyl-CoA) for CMM

(F and G) CMM increases oxidative stress handling capacity in differentiated cardiomyocytes. (F) Representative roGFP2-Grx signal in hiPSC-CMs maintained on CMM or control substrate pulsed with 100 µM H₂O₂, washed out after perfusion, and glutathione pool monitored for 60 s before adding diamide and DTT to obtain maximum and minimum signal, respectively. (G) Quantitative measure showing >80% recovery of glutathione pool on CMM compared with 50% recovery on d30 control. n = 30 in each experimental replicate.

(H and I) Immunoblots of key metabolic enzymes.

Respiration and redox data presented as mean + SEM, and significance calculated by one-way Anova with Tukey's HSD. Immunoblot presented as mean + SD. Statistical significance defined as p < 0.05 (*), p < 0.01 (***), or p < 0.001 (***).



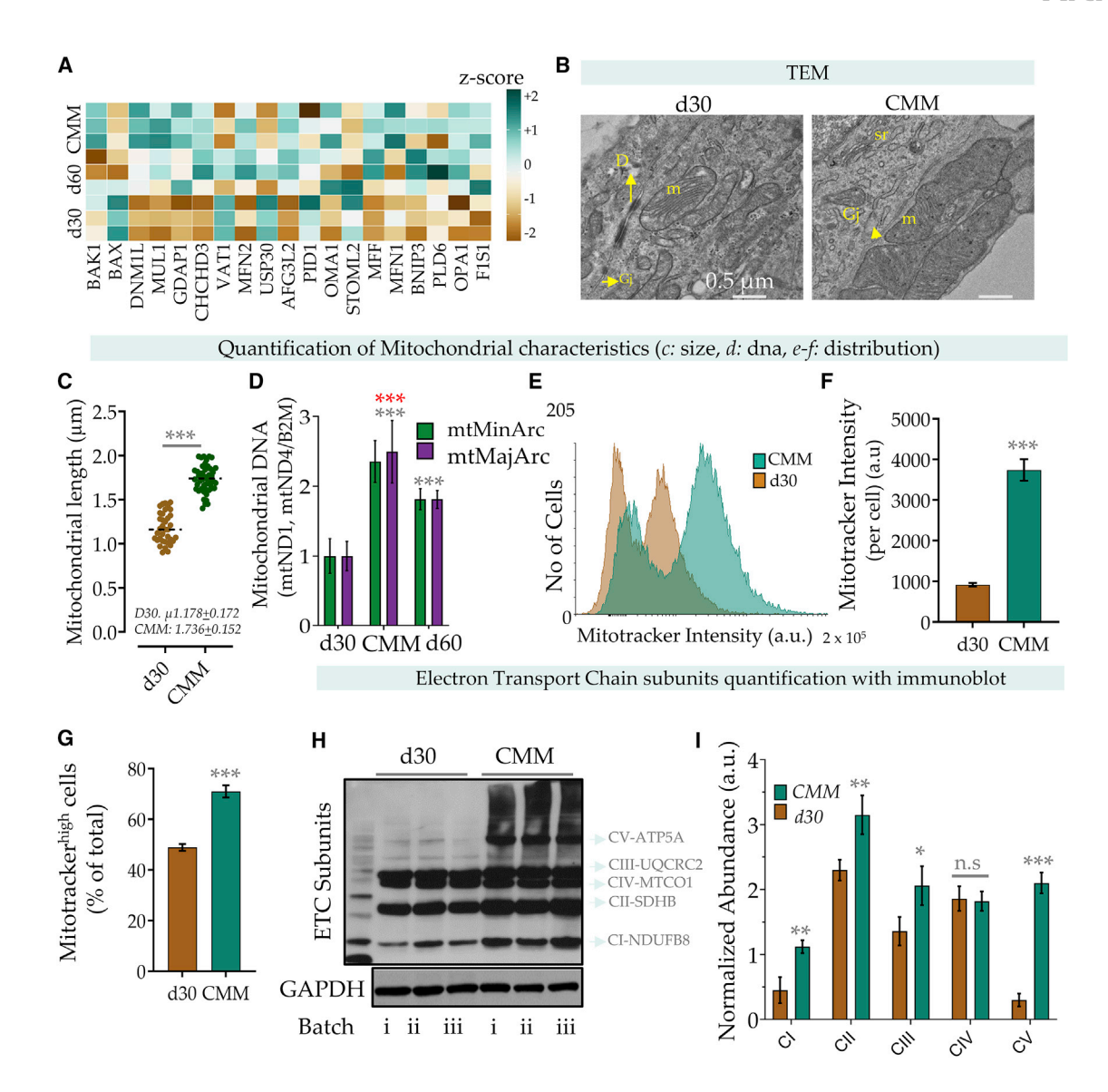


Figure 5. Increase in mitochondrial number and ETC subunits abundance on CMM

- (A) Heatmap showing Z scores of genes involved in mitochondrial dynamics (fusion).
- (B) TEM shows fused elongated mitochondria on CMM. Gj, gap junctions; D, desmosomes; sr, sarcoplasmic reticulum; m, mitochondria.
- (C) Mitochondrial length estimated from longitudinal TEM sections, presented as mean + SD, significance calculated using Wilcoxon test.
- (D) Mitochondrial DNA RT-PCR. Black stars: CMM versus d30; red stars: CMM versus d60, presented as mean + SD, significance calculated by 2-way Anova with Tukev's test.

(E-G) Flow-cytometry analysis of Mitotracker Green (E) indicates >3-fold increase in mitochondrial content on CMM (F) and greater percentage of cells showing high mitochondrial numbers (G), presented as mean + SD.

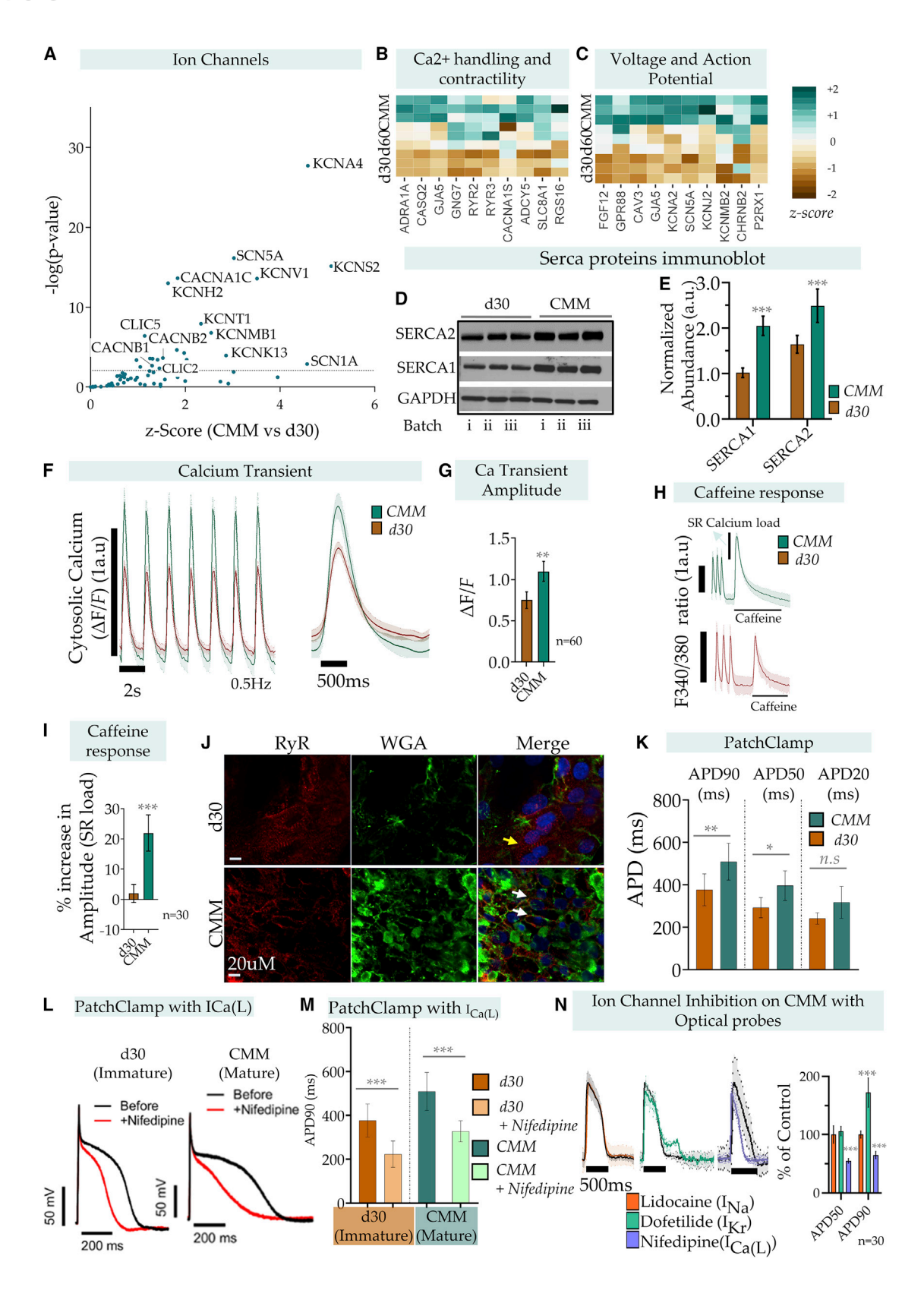
(H and I) Immunoblots of ETC subunits (with relative quantification to GAPDH). Statistical significance is defined as p < 0.05 (*), p < 0.01 (***), or p < 0.001 (****).

(400 nm/485 nm ratio) at 60 s in all the conditions before calibration, and found that cells on CMM showed consistently lower Grx1-roGFP2 ratio (400 nm/485 nm) of 0.423 ± 0.092, indicating rapid recovery of glutathione pool compared with cells on d30 cells (0.7163 \pm 0.08) (Figures 4F and 4G). These results indicate metabolic maturation with higher OxPhos and improved ROS scavenging capability in CMM condition. The metabolic switch was also accompanied by reduced abundance of pyruvate dehydrogenase kinase (PDK1) and platelet

isoform of phosphofructokinase (PFKP), key glycolytic enzyme isoforms that are responsible for aerobic glycolysis, highly expressed in proliferative/glycolytic cells including stem cells (Lunt and Vander Heiden, 2011; Tanner et al., 2018) (Figures 4H and 4I). There was no detectable difference in fatty acid synthase (FAS) levels, but abundance of acetyl-CoA synthetase (AceCS1), an enzyme regulating fatty acid/lipid biosynthesis (Schwer and Verdin, 2008), increased (Figures 4H and 4I).

Article





(legend on next page)





Matured and increased mitochondria in hiPSC-CMs on

To support increased ATP generation from OxPhos, cells require a high mitochondrial number, which are typically fused and elongated in adult cardiomyocytes, as well as upregulation of ETC subunits. MFN1, MFN2, DNM1L, OPA1, and other genes related to mitochondrial fusion were upregulated on CMM (Figure 5A). TEM showed that cells on CMM demonstrate elongated and fused mitochondria (average size 1.73 μm) (Figures 5B and 5C). gRT-PCR of mitochondrial DNA showed >2-fold higher expression in CMM versus d30 or d60 (Figure 5D). Relative per cell mitochondrial content (Mitotracker Green intensity) showed >3-fold higher levels in hiPSC-CMs cultured on CMM versus d30 (Figures 5E and 5F). Interestingly, cells showed two subpopulations with low and high mitochondrial content, the latter significantly enriched on CMM (Figure 5E). As all cells including d30 controls were cTnT+ve (Figure S2), along with the previous data on cTnT and MYL2 distribution these data indicate enrichment of a metabolically and structurally mature ventricular myocyte type phenotype on CMM. We also observed significantly higher levels of key ETC subunits (I, II, III) and ATP synthase (subunit V) in cells on CMM in three biological replicates, although protein expression levels for subunit IV were not different (Figures 5H, 5I, and S11). These results demonstrate that CMM induces increases in mitochondrial content, structural maturation, and quality.

Improved electrophysiological and calcium transient on

Cardiac tissue development leads to coordinated electrical excitation coupled to contraction known as excitation contraction coupling (ECC) (Bers, 2002). The interplay of ions for ECC requires specific expression of proteins including L-type Ca2+ channels (LTCC), ryanodine receptors, sarcoplasmic/ER Ca2+ ATPase (SERCA), and Na⁺/Ca²⁺ exchanger (Bers, 2002; Liu et al., 2016), Cardiac maturation on CMM led to a synchronous but slow beating rate of cells (Figures 3O, S10F, and S10G) (Keung et al., 2014; Sartiani et al., 2007). CMM showed significant upregulation of several ion channel transcripts present in developed myocytes (Figure 6A). Channel components encoded by these genes are involved in rapid upstroke (SCNA5: encodes Nav1.5) and phase 1 of repolarization (Kv1.4: KCNA4). Several key calcium handling genes including L-type calcium channels

(LTCC), ryanodine receptors (RyR), calsequestrin (Casq2), and phospholamban (Pln) were also upregulated, indicating better maturation on CMM even compared with d60 (Figures 6B and 6C).

Efficient calcium cycling is crucial to convert electrical signals to mechanical force in the myocytes (Bers, 2002), and calcium transient profiles inform the extent of maturation (Liu et al., 2009). SERCA had higher abundance in CMM versus control (Figures 6D and 6E). Using GCamp6f, we found higher Ca²⁺ transient amplitude ($\Delta F/F$) in CMM compared with d30 (Figures 6F and 6G). To evaluate calcium handling efficiency, we investigated caffeine-induced Ca2+ release from the SR for calcium storage (SR load) using 10 mM caffeine in Fura2 (ratiometric dye)-loaded cells (Feyen et al., 2020). Cells matured on CMM demonstrated increased calcium decay time and calcium amplitude, and a significant increase in amplitude following caffeine exposure, while d30 cells failed to demonstrate the calcium release from SR (Figures 6H, 6I, S12A, and S12B; Videos S3, S4, S5, S6, S7, S8, S9, S10, S11, S12, and S13). Ryanodine receptors (RYR2), a Ca2+-induced Ca2+ release (CICR) modulator, were also localized near the WGA-labeled membranes with low cytoplasmic localization in CMM compared with d30 (Figure 6J).

We then performed single-cell patch clamping and found that CMM significantly increased action potential duration (APD) APD90 and APD50 versus d30 (Figures 6K and S10C). No statistical difference was observed between d30 and CMM on maximum diastolic potential (MDP) and AP amplitude, which was about -70 mV and 170 mV, respectively (Figure S10C). We observed significant reduction in time to peak (5.22 ms versus 9.78 ms) and maximum depolarization rate (MDR) in cells on CMM compared with d30 cells (Figure S10C). We obtained similar APD profiles with genetically encoded voltage indicators (Jin et al., 2012; Kannan et al., 2018), which exhibited the APD90 of 436.4 \pm 6.71 ms compared with 345.6 \pm 6.23 ms in d30 cells at 1 Hz and 485.3 \pm 13.80 ms compared with 371.1 \pm 18.89 ms in d30 cells at 0.5 Hz (Barbuti et al., 2016) (Figures S10D-S10G). We investigated the effect of 100 nM nifedipine, an L-type Ca²⁺ channel blocker, using patch clamping and found significant reduction of APD90 on both, with greater response in cells on CMM (Figures 6L and 6M). We then performed a comprehensive ion channel inhibition on cells matured on CMM (Figures 6N and S10H-S10K). Lidocaine, a sodium channel blocker, reduced the frequency (by \sim 40% in two biological batches; n = 30)

Figure 6. CMM improves calcium handling and electrophysiological maturation

(A) Ion channels with increased expression in CMM compared with d30.

(B and C) (B) Calcium handling and (C) voltage and action potential-related genes with increased expression in CMM versus d30.

(D and E) Immunoblots of SERCA proteins.

(F and G) Calcium transient of cells in CMM and d30 using GCamp6f. Normalized calcium traces and a representative normalized trace of calcium indicated higher transient amplitude on CMM, presented as mean + SD.

(H and I) Sarcoplasmic reticulum (SR) calcium content using ratiometric Fura2 imaging. Caffeine (10 mM) exposure shows significant calcium release from CMM cells, presented as mean + SD.

(J) Immunostaining of RYR2 and membrane labeling with WGA. White arrows show RYR2 on CMM, and yellow arrow indicates cytoplasmic RYR2 in d30.

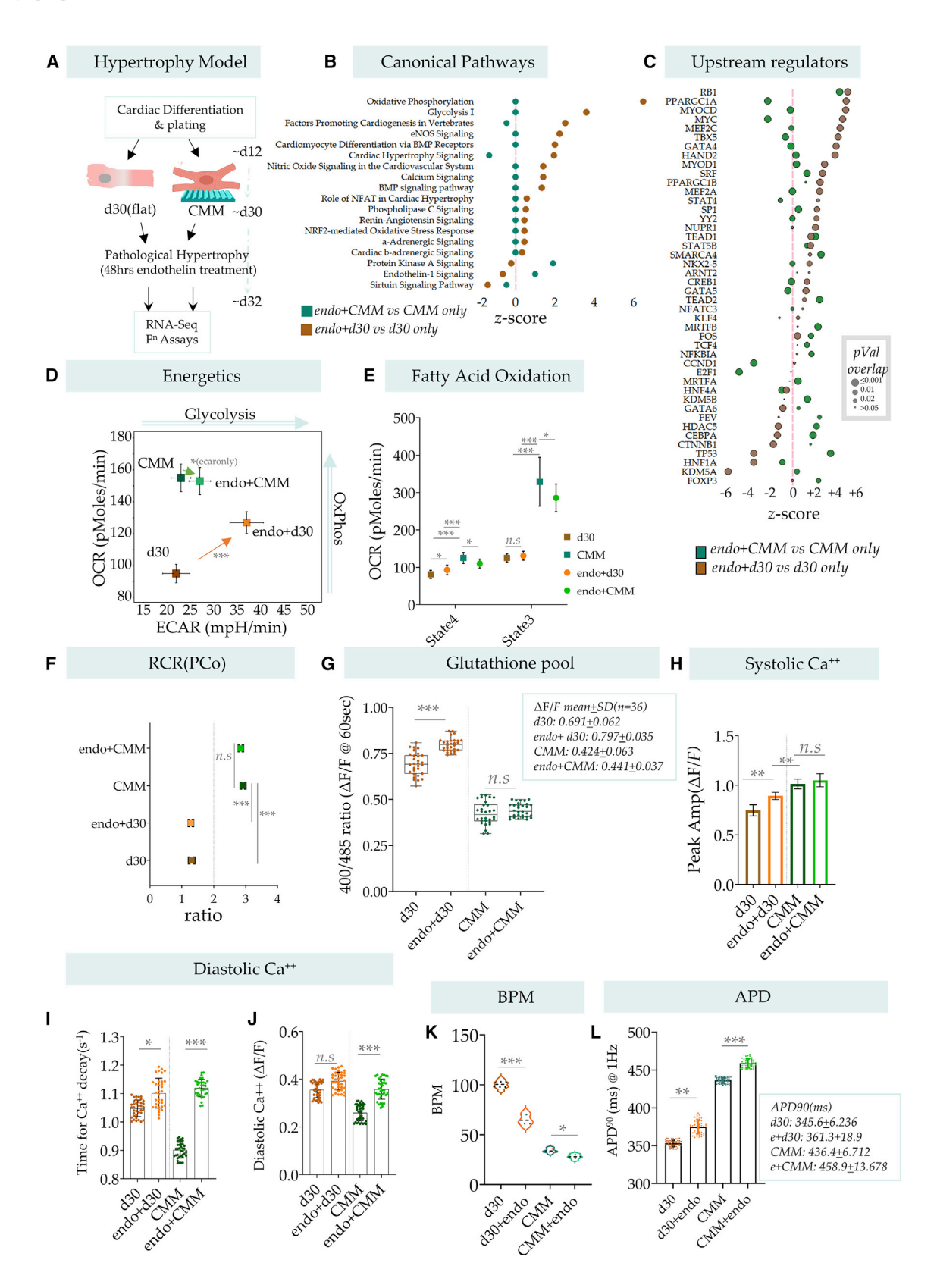
(K-M) Electrophysiological patch-clamp analysis. (K) Increase APD50 and APD90 in cells in CMM versus d30. (L and M) Cells on CMM were more responsive to calcium channel (Ca_L) inhibition using nifedipine (I_{Ca(L)} 100 nM).

(N) Response to ion channel inhibitors in cells on CMM using optical recording of action potential with Varnam probe. Averaged single AP traces show that cells on CMM respond to ion channel inhibitors: lidocaine (I_{Na} 100 µM), dofetilide (I_{Kr} 3 nM), Nifedipine (I_{Ca(L)} 100 nM). For calcium and AP data, x axis (time) and y axis (intensity) are scaled/normalized to same unit for both CMM and d30 to represent them together. (F), (H), (L), and (N) have units defined by black bars.

Cell Reports Article







(legend on next page)





(Figures 6N and S10H), while potassium channel inhibition by dofetilide induced AP prolongation and early after depolarization (Figures 6N and S10I). Dofetilide is a well-characterized drug associated with corrected QT interval prolongation and torsades de pointes, and is a human ether-a-go-go-related gene (hERG) K+ channel blocker used to evaluate maturity of iPSC-CMs for their utility in cardiotoxicity screens (Shi et al., 2020). Cells on CMM were sensitive to a 3 nM dose of dofetilide while they failed to tolerate the 10 nM dose range (Figure S10J). Nifedipine reduced the AP duration (APD50, APD90) without affecting frequency (Figures 6N and S10K). These results indicate significant electrophysiological maturation of cells on CMM.

CMM mitigates the response of pathological hypertrophy induction

With establishment of transcriptional, metabolic, redox, and calcium handling characteristics of a matured cardiac tissue, we tested the effect of a key pathological stimulus, endothelin-1 (ET-1) treatment, on cardiac cells (Figure 7A). Endothelin mediates a wide range of effects on cardiac tissue, with an increase in muscle size and abnormalities in cellular contractility, and calcium dynamics resulting in pathological hypertrophy (Archer et al., 2017). Like most cardiac diseases, pathological hypertrophy is a slowly progressing disease resulting from chronic elevated workload on the heart, resulting in cardiac remodeling without myocyte proliferation and gradual disruption of normal matrix architecture (Marian and Braunwald, 2017; Rossi, 1998), which itself accentuates and accelerates disease progression (Kim et al., 2000; Sewanan et al., 2019). We surmised that culture of hiPSC-CMs on non-physiological architecture (d30) may prime cells to be more sensitive to ET-1-induced pathological hypertrophy. We treated both d30 and CMM constructs with ET-1 for 48 h, and profiled gene expression using RNA sequencing. ET-1 samples were compared with their own respective untreated control samples (d30 or CMM), as the maturation state of cells is expected to be different in either matrix context (Figure 7A).

Using IPA pathway analysis, we found that ET-1 treatment in d30 exhibited differential regulation of gene expression related to adrenergic signaling, metabolism, hypertrophic signaling, calcium, and nitric oxide synthase signaling (Figure 7B), while the effect on CMM was attenuated. While ET-1 downstream signaling targets and protein kinase A signaling were upregulated in CMM after ET-1 treatment, the metabolic effect was -minimal (Figure 7B). IPA analysis predicted activation of key cardiac-specific TFs related to cardiogenesis, metabolic transformation, and hypertrophy on d30, including GATA4/5, MYOD1, PPARG, TBX5, MEF2A, MYOC, and MYOD1 (Figure 7C). ET-1 treatment increased enrichment of these gene ontologies; their levels were still not similar to those of CMM, which activates maturation-related ontologies (calcium, metabolism, electrophysiology) (Figure 2C). Overall, these data indicate that ET-1-induced hypertrophy is partly attenuated by the presence of physiological matrix, or, conversely, the lack of cardiac-specific matrix supports progression of pathological hypertrophy. We confirmed this observation by comparing published human gene expression data from hypertrophic myectomy samples (NCBI GEO: GSE6961) from patients with established disease phenotype, and therefore expected remodeled hearts (Figures S13 and S14). Diseased transcripts were compared with their own controls (Figures S13 and S14). We found several key transcripts showing similar response in hypertrophic cardiomyopathy patients and d30 with ET-1 treatment including tricarboxylic acid cycle and expression of Nppa compared with CMM (Figure S13A). Using non-parametric-based gene set enrichment analysis, we found that transcripts that were downregulated in hypertrophic cardiomyopathy patients showed opposite enrichment in CMM after ET-1 treatment compared with d30, while no discernible difference was observed in upregulated genes (Figures S13B and S13C). Furthermore, we used single-cell RNA sequencing data from a published angiotensin mouse model (McLellan et al., 2020) and found that several transcripts are differentially regulated in both the mouse model and d30 after ET-1 treatment compared with CMM. These transcripts included Nppa and those encoding ETC subunits (Figure S14).

We then proceeded to confirm the attenuated response of ET-1 on hiPSC-CMs matured on CMM for key characteristics of cardiac function: metabolism (energetics and redox), calcium handling, and electrophysiology. ET-1 treatment significantly increased both OxPhos and glycolysis on d30, but the levels of OxPhos was still lower than cells on CMM (Figure 7D). After ET-1 treatment, cells on d30 exhibited an increase in FAO while CMM exhibited an opposite effect (Figure 7E). Although respiratory control ratio (state-3 [active] respiration to state-4 [basal] respiration) was higher in CMM, it was not affected upon acute ET-1 treatment (Figure 7F). Taken together, upon ET-1 treatment CMM exhibited a metabolic response of slight increase in glycolysis, with reduction in FAO, and modest response to induction of pathological hypertrophy (de las Fuentes et al., 2003; Kolwicz and Tian, 2011; Lopaschuk et al., 2010). roGFP2 after H₂O₂ treatment showed d30 cells to have reduced oxidative stress handling with ET-1, while it was unperturbed in CMM (Figure 7G). Ca2+ levels showed an increase in peak amplitude on d30 with ET-1, but no significant effect on CMM (Figure 7H), with increased Ca²⁺ delay in both conditions, primarily by an increase in the diastolic calcium

Figure 7. Cardiac ultrastructure attenuates pathological hypertrophy phenotype

(A) Schematic showing acute pathological hypertrophy model.

(B and C) RNA sequencing analysis of ET-1 treatment. (B) Canonical pathways (IPA) in ET-1 treated d30 and CMM compared with their respective untreated conditions. (C) Key transcriptional regulators affected by ET-1 treatment in d30 and CMM.

(D-L) Functional evaluation of ET-1 effect on d30 and CMM cells. (D) Increase in OxPhos and glycolysis in d30 cells while cells on CMM exhibit slight increase in glycolysis with no effect on OxPhos. (E) Reduction in FAO with hypertrophy induction on CMM (n = 6). (F) Respiratory control ratio (state 3/state 4) of FAO. Respiratory ration data presented as mean + SEM, significance calculated using one-way Anova with Tukey's HSD. (G) Measure of glutathione pool, presented as mean + SD. (H) Systolic and (I and J) diastolic calcium measurements, presented as mean + SD. (K) Beating frequency (beats per minute), presented as mean+SD. (L) APD measured as time duration between 10% and 90% of peak values, presented as mean + SD. Statistical significance is defined as p < 0.05 (*), p < 0.01 (***), or p < 0.001 (****).

Article



levels for CMM upon ET-1 stimulation (Figures 7I and 7J). Finally, we found a decrease in beating frequency (Figure 7K) and increase in AP duration (Figure 7I) for both d30 and CMM. Together, these data, along with our earlier findings establishing the increased maturation of cardiomyocytes on CMM, show that a physiologically intact matrix and the resultant cardiomyocyte state can attenuate the pathological manifestation of endothelin treatment, particularly withstanding the disruption in metabolism and redox handling, while electrophysiological effects of the treatment continue to manifest. Conversely, these data indicate that disrupted matrix architecture due to hypertrophic remodeling possibly contributes to the disease progression itself.

DISCUSSION

Recognized failure of small animals as models for cardiac diseases and drug screening due to discernible differences from humans in calcium handling, electrophysiological characteristics, and metabolism has resulted in increased recognition for the need of human cardiac constructs in the preclinical setting (Gintant et al., 2019). Our protocol utilizes the synergistic effect of chemical and mechanical parameters of the adult heart matrix to accelerate maturation of differentiated cardiomyocytes toward a more mature state. We found that maintenance of differentiated cardiomyocytes on CMM (for 15-18 days) could generate a construct nearly 50% transcriptomically closer to the adult heart in comparison with well-differentiated control cultures (baseline comparing well with recent studies). Notably, CMM resulted in more mature tissue than the standard monolayer prolonged culture of 60 days, suggesting accelerated maturation.

Extensive characterizations demonstrate that hiPSC-CMs matured on CMM show substantial structural, mechanical, and electrophysiological maturation. Matured constructs on CMM exhibit structurally developed sarcomere structures, a switch from myosin light chain-7 (MYL7) to MYL2, and increased abundance of cTnT and cTnI isoforms. We augmented CMM with TFM to directly measure cardiac contractility and electromechanical coupling, finding that cells on CMM were two to three times more contractile than d30 control. hiPSC-CMs demonstrate maturation in calcium transients and electrophysiological parameters and sensitivity to various ion channel blockers, demonstrating their utility for electrophysiological screens.

A key feature of cardiac maturation is the switch in energy metabolism leading to an increase in mitochondrial respiration (Ahmed et al., 2020; Correia et al., 2017). Adult heart is known to be rich with mitochondria (30% of cardiomyocyte volume) (Barth et al., 1992), with high metabolic requirement/substrate utilization (including medium-/long-chain fatty acids) and oxygen consumption, invariably leading to higher ROS generation, necessitating sophisticated redox balancing modules (Madamanchi and Runge, 2013). A detailed investigation of mitochondrial energetics (in intact and permeabilized cardiac cells) indicated higher oxygen consumption, coupled respiration, and state-3/ADP-stimulated respiration. These data, along with abundance of ETC subunits, suggest that CMM led to an increase in mitochondrial number and their competence (Liu et al., 2011) (Figures 4 and 5). We found a concomitant increase in FAO, indicating a switch toward higher β -oxidation, a hallmark of cardiac maturation (Doenst et al., 2013) (Figure 4E). We also observed a significant increase in oxidative stress handling capability with cardiac maturation (Figure 4G). In the light of the importance of metabolism in most cardiac pathologies, and many drug toxicities (Madamanchi and Runge, 2013; Santos et al., 2011), enhanced redox handling capability and higher ETC function and competence can be utilized as comprehensive metabolic milestones of maturation.

A key overlooked aspect of cardiac maturation and disease modeling is the role of cardiac ultrastructure in the pathological progression of disease. In vitro disease models mostly focus on established cardiac diseases in which cardiac ultrastructure is invariably disrupted (Marian and Braunwald, 2017). Pathological hypertrophy is a gradually progressing disease, resulting from chronic and aberrant cardiac workload that remodels the heart tissue, itself feeding into the disease progression (Marian and Braunwald, 2017). Comparing phenotype data from hypertrophied patients and mouse model single-cell RNA sequencing, we found key gene ontologies similarly upregulated in d30 samples without cardiac mimicking matrix architecture. Transcriptomic, metabolic, and electrophysiological readouts confirmed that cardiac-specific matrix's effect on hiPSC-CMs allows them to partly mitigate the effect of ET-1 induction. These results highlight the need to dissect pathological disease progression in similarly mature cells on physiological cardiac ultrastructure versus disrupted ultrastructure to broaden our understanding of hypertrophic cardiomyopathy, heart failure, or other cardiac

CMM combines ligand chemistry, elasticity, and anisotropic ultrastructure of the stromal matrix within the heart in a highly scalable, inexpensive, reproducible, and convenient platform. We utilized an unconventional approach to identify the ligands using transcriptomic analysis of adult heart tissue, which may more accurately reflect the ligands to which heart cells actually respond from a much larger cohort of ligands in the heart matrix. We also show that anisotropic nanowrinkled ultrastructure, closely mimicking natural heart collagen matrix architecture compared with simply parallel nanoridges (Carson et al., 2016) or other methods (Kumar et al., 2020), along with cardiac-specific rigidity induces cardiac-specific gene expression and mitochondrial content. Other methodological advances include measurement of traction force generation by paced cells on anisotropic nanowrinkled hydrogel, and a hybrid Steiner tree network approach to identify potential signaling intermediaries connecting the stimulus to the target genes. The systemic perturbation of signaling intermediaries will open new lines of enquiry into understanding the mechanisms underlying matrix-mediated cardiac

Recent engineered approaches to mature differentiated cardiac cells, using 3D tissue-culture and monolayer systems, have shown dramatic advances in calcium response, contractility, and electrophysiological parameters (Guo and Pu, 2020; Tu et al., 2018; Weinberger et al., 2017). Although engineered tissue approaches provide benefits over the above parameters, the flexibility, scalability, and reproducibility of a monolayer culture system in addition to their utility for organelle/cellular-level





investigation is still unparalleled. Organelle assessment such as ETC function or crosstalk, even with recognized caveats (Picard et al., 2011), is still dependent on fractionated organelle studies due to a lack of similar investigation capabilities at the tissue level. Matured myocytes on a monolayer can offer similar flexibility without the disadvantages of mitochondrial isolation using non-permeabilized and/or permeabilized cells. Lack of mature reductive platforms provided by monolayers has limited investigations into live dynamics of organelle, signaling, molecular, and bioenergetic pathways. The flexibility and scalability of a monolayer system is complementary to a 3D construct, thus offering a possibility for comprehensive evaluation of the cardiac system, such as seen with an adult animal heart model-at the tissue, in individual myocytes, and on an organelle level. Overall, our platform to accelerate maturation of hiPSC-CMs toward an adult-like state presents a convenient method to create cell resources for downstream applications in toxicity screens, as well as to delineate mechanisms regulating cardiac phenotypes, including electrophysiology, contractility, metabolism, energetics, and oxidative stress management.

Limitations of the study

To obtain a comparative understanding of the TFM data under d30 and CMM conditions, cells in both conditions were dissociated and replated on anisotropic nano-TFM surfaces. Notably, d30 condition is isotropic and will likely result in even lower strain energy in isotropic TFM. Similarly, XF analyzer studies were performed after dissociation and replating the cells to maintain similar cell density/spreading for experiments, and the assay media contained supplements to mimic culture environment. This may have mitigated differences in the energetic parameters between d30 and CMM. Incorporation of CMM directly in XF analyzer studies is a desirable goal, as well as incorporation of other microenvironmental factors on which many groups are experimenting. We would also re-emphasize that cultures on standard tissue-culture surfaces (d30) and CMM have different status of cardiac maturation, which may affect the phenotype in response to ET-1 treatment in iPSC-CMs.

STAR*METHODS

Detailed methods are provided in the online version of this paper and include the following:

- KEY RESOURCES TABLE
- RESOURCE AVAILABILITY
 - Lead contact
 - Materials availability
 - Data and code availability
- METHOD DETAILS
 - O Human iPSC culture and cardiac differentiation
 - Fabrication of nanowrinkled molds for cardiac mimetic matrix
 - Fabrication of cardiac mimetic matrix substrates
 - Functionalization of CMM and Raman spectroscopy
 - O RT-PCR
 - Mitochondrial number
 - RNA sequencing and analysis

- Immunostaining
- O Confocal and airyscan imaging
- Flow cytometry
- Immunoblots
- Mitochondrial respiration
- Particle image velocimetry (PIV) analysis
- Transmission Electron Microscopy
- Traction Force Microscopy
- O Cyto-calcium, action potential and redox handling
- O Steiner tree based protein-protein interaction map
- Patch clamp electrophysiology
- QUANTIFICATION AND STATISTICAL ANALYSIS

SUPPLEMENTAL INFORMATION

Supplemental information can be found online at https://doi.org/10.1016/j. celrep.2022.111146.

ACKNOWLEDGMENTS

We would like to thank Dr. David Pollard, Yale University, for use of his Airyscan super-resolution microscope setup. We would also like to thank Dr. Brian O'Rourke, Johns Hopkins University, for his valubale insights and guidance. We also extend our acknowledgments to the funding from American Heart Association innovation grant (16IRG27260356, 17IRG33460364), and University of Connecticut Biomedical Engineering startup for completion of the manuscript. A.D. used funding from her NSF CAREER grant (2044870) for Raman microscopy.

AUTHOR CONTRIBUTIONS

J.A. and K.K. conceived the manuscript, designed the experiments, supervised the project, and wrote the manuscript; J.A., Y.L., Y.S., and K.K. performed energetics/redox experiments, immunoblots, optical imaging experiments, and bioinformatics analysis; W.D. created the CMM matrix and performed TFM; P.Z. and J.F. performed patch-clamp electrophysiological experiments; V.A. performed particle velocimetry; W.A.S. performed Airyscan; J.N. performed AFM; M.Y. performed TEM; A.C.D. provided Raman spectroscopy; L.Y. oversaw electrophysiological experiments; K.K. oversaw the project.

DECLARATION OF INTERESTS

K.K., J.A., W.D., and Y.S. are inventors on a provisional patent filed describing the technology in this paper. K.K. is an inventor of a licensed patent to CuriBio, Inc. (9,994,812), whose products were used for comparative purposes during the review process.

Received: March 20, 2022 Revised: April 26, 2022 Accepted: July 7, 2022 Published: July 26, 2022

REFERENCES

Afzal, J., Chan, A., Karakas, M.F., Woldemichael, K., Vakrou, S., Guan, Y., Rathmell, J., Wahl, R., Pomper, M., Foster, D.B., et al. (2017). Cardiospherederived cells demonstrate metabolic flexibility that is influenced by adhesion status. JACC. Basic Transl. Sci. 2, 543-560.

Ahmed, R.E., Anzai, T., Chanthra, N., and Uosaki, H. (2020). A brief review of current maturation methods for human induced pluripotent stem cells-derived cardiomyocytes. Front. Cell Dev. Biol. 8, 178.

Article



Akhmedov, M., LeNail, A., Bertoni, F., Kwee, I., Fraenkel, E., and Montemanni, R. (2017). A fast prize-collecting steiner forest algorithm for functional analyses in biological networks. Lect. Notes Comput. Sc. 10335, 263-276.

Aquilano, K., Baldelli, S., and Ciriolo, M.R. (2014). Glutathione: new roles in redox signaling for an old antioxidant. Front. Pharmacol. 5, 196.

Aratyn-Schaus, Y., Oakes, P.W., Stricker, J., Winter, S.P., and Gardel, M.L. (2010). Preparation of complaint matrices for quantifying cellular contraction. J. Vis. Exp., 2173. https://doi.org/10.3791/2173.

Archer, C.R., Robinson, E.L., Drawnel, F.M., and Roderick, H.L. (2017). Endothelin-1 promotes hypertrophic remodelling of cardiac myocytes by activating sustained signalling and transcription downstream of endothelin type A receptors. Cell. Signal. 36, 240-254.

Avad. N.M.E., Kaushik, S., and Weaver, V.M. (2019), Tissue mechanics, an important regulator of development and disease. Philos. Trans. R. Soc. Lond. B Biol. Sci. 374, 20180215.

Barbuti, A., Benzoni, P., Campostrini, G., and Dell'Era, P. (2016). Human derived cardiomyocytes: a decade of knowledge after the discovery of induced pluripotent stem cells. Dev. Dynam. 245, 1145-1158.

Barth, E., Stämmler, G., Speiser, B., and Schaper, J. (1992). Ultrastructural quantitation of mitochondria and myofilaments in cardiac muscle from 10 different animal species including man. J. Mol. Cell. Cardiol. 24, 669-681.

Bedada, F.B., Wheelwright, M., and Metzger, J.M. (2016). Maturation status of sarcomere structure and function in human iPSC-derived cardiac myocytes. Biochim. Biophys. Acta 1863, 1829-1838.

Bers, D.M. (2002). Cardiac excitation-contraction coupling. Nature 415, 198-205

Bienstock, D., Goemans, M.X., Simchilevi, D., and Williamson, D. (1993). A note on the prize collecting traveling salesman problem. Math. Program. 59, 413-420.

Burgoyne, J.R., Mongue-Din, H., Eaton, P., and Shah, A.M. (2012). Redox signaling in cardiac physiology and pathology. Circ. Res. 111, 1091–1106.

Burridge, P.W., Matsa, E., Shukla, P., Lin, Z.C., Churko, J.M., Ebert, A.D., Lan, F., Diecke, S., Huber, B., Mordwinkin, N.M., et al. (2014). Chemically defined generation of human cardiomyocytes. Nat. Methods 11, 855-860.

Carson, D., Hnilova, M., Yang, X., Nemeth, C.L., Tsui, J.H., Smith, A.S.T., Jiao, A., Regnier, M., Murry, C.E., Tamerler, C., and Kim, D.H. (2016). Nanotopography-induced structural anisotropy and sarcomere development in human cardiomyocytes derived from induced pluripotent stem cells. ACS Appl. Mater. Interfaces 8, 21923-21932.

Caulfield, J.B., and Janicki, J.S. (1997). Structure and function of myocardial fibrillar collagen. Technol. Health Care 5, 95-113.

Chen, T.W., Wardill, T.J., Sun, Y., Pulver, S.R., Renninger, S.L., Baohan, A., Schreiter, E.R., Kerr, R.A., Orger, M.B., Jayaraman, V., et al. (2013). Ultrasensitive fluorescent proteins for imaging neuronal activity. Nature 499, 295–300.

Cho, G.S., Lee, D.I., Tampakakis, E., Murphy, S., Andersen, P., Uosaki, H., Chelko, S., Chakir, K., Hong, I., Seo, K., et al. (2017). Neonatal transplantation confers maturation of PSC-derived cardiomyocytes conducive to modeling cardiomyopathy. Cell Rep. 18, 571-582.

Choi, J.S., Smith, A.S.T., Williams, N.P., Matsubara, T., Choi, M., Kim, J.W., Kim, H.J., Choi, S., and Kim, D.H. (2020). Nanopatterned Nafion microelectrode arrays for in vitro cardiac electrophysiology. Adv. Funct. Mater. 30,

Choy, J.Y.H., Boon, P.L.S., Bertin, N., and Fullwood, M.J. (2015). A resource of ribosomal RNA-depleted RNA-Seq data from different normal adult and fetal human tissues, Sci. Data 2, 150063.

Correia, C., Koshkin, A., Duarte, P., Hu, D., Teixeira, A., Domian, I., Serra, M., and Alves, P.M. (2017). Distinct carbon sources affect structural and functional maturation of cardiomyocytes derived from human pluripotent stem cells. Sci.

Crowder, S.W., Liang, Y., Rath, R., Park, A.M., Maltais, S., Pintauro, P.N., Hofmeister, W., Lim, C.C., Wang, X., and Sung, H.J. (2013). Poly(epsilon-caprolactone)-carbon nanotube composite scaffolds for enhanced cardiac differentiation of human mesenchymal stem cells. Nanomedicine (Lond) 8, 1763-1776

de las Fuentes, L., Herrero, P., Peterson, L.R., Kelly, D.P., Gropler, R.J., and Dávila-Román, V.G. (2003). Myocardial fatty acid metabolism: independent predictor of left ventricular mass in hypertensive heart disease. Hypertension 41, 83-87.

Dias, T.P., Pinto, S.N., Santos, J.I., Fernandes, T.G., Fernandes, F., Diogo, M.M., Prieto, M., and Cabral, J.M.S. (2018). Biophysical study of human induced Pluripotent Stem Cell-Derived cardiomyocyte structural maturation during long-term culture. Biochem. Biophys. Res. Commun. 499, 611-617.

Doenst, T., Nguyen, T.D., and Abel, E.D. (2013). Cardiac metabolism in heart failure: implications beyond ATP production. Circ. Res. 113, 709-724.

Feaster, T.K., Cadar, A.G., Wang, L., Williams, C.H., Chun, Y.W., Hempel, J.E., Bloodworth, N., Merryman, W.D., Lim, C.C., Wu, J.C., et al. (2015). Matrigel mattress: a method for the generation of single contracting human-induced pluripotent stem cell-derived cardiomyocytes. Circ. Res. 117, 995-1000.

Feyen, D.A.M., McKeithan, W.L., Bruyneel, A.A.N., Spiering, S., Hörmann, L., Ulmer, B., Zhang, H., Briganti, F., Schweizer, M., Hegyi, B., et al. (2020). Metabolic maturation media improve physiological function of human iPSC-derived cardiomyocytes, Cell Rep. 32, 107925.

Fischer, R.S., Myers, K.A., Gardel, M.L., and Waterman, C.M. (2012). Stiffnesscontrolled three-dimensional extracellular matrices for high-resolution imaging of cell behavior. Nat. Protoc. 7, 2056-2066.

Friedman, C.E., Nguyen, Q., Lukowski, S.W., Helfer, A., Chiu, H.S., Miklas, J., Levy, S., Suo, S., Han, J.D.J., Osteil, P., et al. (2018). Single-cell transcriptomic analysis of cardiac differentiation from human PSCs reveals HOPX-dependent cardiomyocyte maturation. Cell Stem Cell 23, 586-598.e8.

Gintant, G., Burridge, P., Gepstein, L., Harding, S., Herron, T., Hong, C., Jalife, J., and Wu, J.C. (2019). Use of human induced pluripotent stem cell-derived cardiomyocytes in preclinical cancer drug cardiotoxicity testing: a scientific statement from the American heart association, Circ. Res. 125, e75-e92.

Goversen, B., van der Heyden, M.A.G., van Veen, T.A.B., and de Boer, T.P. (2018). The immature electrophysiological phenotype of iPSC-CMs still hampers in vitro drug screening: special focus on Ik1. Pharmacol. Ther. 183,

Guo, Y., and Pu, W.T. (2020). Cardiomyocyte maturation: new phase in development. Circ. Res. 126, 1086-1106.

Gutscher, M., Pauleau, A.L., Marty, L., Brach, T., Wabnitz, G.H., Samstag, Y., Meyer, A.J., and Dick, T.P. (2008). Real-time imaging of the intracellular glutathione redox potential. Nat. Methods 5, 553-559.

Harris, M.A., Clark, J., Ireland, A., Lomax, J., Ashburner, M., Foulger, R., Eilbeck, K., Lewis, S., Marshall, B., Mungall, C., et al. (2004). The Gene Ontology (GO) database and informatics resource. Nucleic Acids Res. 32, D258-D261.

He, C., Hu, H., Wilson, K.D., Wu, H., Feng, J., Xia, S., Churko, J., Qu, K., Chang, H.Y., and Wu, J.C. (2016). Systematic characterization of long noncoding RNAs reveals the contrasting coordination of cis- and trans-molecular regulation in human fetal and adult hearts. Circ. Cardiovasc. Genet. 9, 110-118.

Hom, J.R., Quintanilla, R.A., Hoffman, D.L., de Mesy Bentley, K.L., Molkentin, J.D., Sheu, S.S., and Porter, G.A., Jr. (2011). The permeability transition pore controls cardiac mitochondrial maturation and myocyte differentiation. Dev. Cell 21, 469-478.

Hu. D., Linders, A., Yamak, A., Correia, C., Kiilstra, J.D., Garakani, A., Xiao, L., Milan, D.J., van der Meer, P., Serra, M., et al. (2018). Metabolic maturation of human pluripotent stem cell-derived cardiomyocytes by inhibition of HIF1alpha and LDHA. Circ. Res. 123, 1066-1079.

Hubbi, M.E., Kshitiz, Gilkes, D.M., Gilkes, D.M., Rey, S., Wong, C.C., Luo, W., Kim, D.H., Dang, C.V., Levchenko, A., and Semenza, G.L. (2013). A nontranscriptional role for HIF-1alpha as a direct inhibitor of DNA replication. Sci. Signal. 6, ra10.

Huntley, R.P., Sawford, T., Mutowo-Meullenet, P., Shypitsyna, A., Bonilla, C., Martin, M.J., and O'Donovan, C. (2015). The Goa database: gene Ontology annotation updates for 2015. Nucleic Acids Res. 43, D1057-D1063.



Ingwall, J.S. (2009). Energy metabolism in heart failure and remodelling. Cardiovasc. Res. 81, 412-419.

Jin, L., Han, Z., Platisa, J., Wooltorton, J.R.A., Cohen, L.B., and Pieribone, V.A. (2012). Single action potentials and subthreshold electrical events imaged in neurons with a fluorescent protein voltage probe. Neuron 75, 779-785.

Jung, J.P., Hu, D., Domian, I.J., and Ogle, B.M. (2015). An integrated statistical model for enhanced murine cardiomyocyte differentiation via optimized engagement of 3D extracellular matrices. Sci. Rep. 5, 18705.

Kaiser, N.J., Kant, R.J., Minor, A.J., and Coulombe, K.L.K. (2019). Optimizing blended collagen-fibrin hydrogels for cardiac tissue engineering with human iPSC-derived cardiomyocytes. ACS Biomater. Sci. Eng. 5, 887-899.

Kannan, M., Vasan, G., Huang, C., Haziza, S., Li, J.Z., Inan, H., Schnitzer, M.J., and Pieribone, V.A. (2018). Fast, in vivo voltage imaging using a red fluorescent indicator. Nat. Methods 15, 1108-1116.

Karakikes, I., Ameen, M., Termglinchan, V., and Wu, J.C. (2015). Human induced pluripotent stem cell-derived cardiomyocytes: insights into molecular, cellular, and functional phenotypes. Circ. Res. 117, 80-88.

Kedaigle, A.J., and Fraenkel, E. (2018). Discovering altered regulation and signaling through network-based integration of transcriptomic, epigenomic and proteomic tumor data. Methods Mol. Biol. 1711, 13-26.

Keung, W., Boheler, K.R., and Li, R.A. (2014). Developmental cues for the maturation of metabolic, electrophysiological and calcium handling properties of human pluripotent stem cell-derived cardiomyocytes. Stem Cell Res. Ther. 5, 17.

Khan, M., Xu, Y., Hua, S., Johnson, J., Belevych, A., Janssen, P.M.L., Gyorke, S., Guan, J., and Angelos, M.G. (2015). Evaluation of changes in morphology and function of human induced pluripotent stem cell derived cardiomyocytes (HiPSC-CMs) cultured on an aligned-nanofiber cardiac patch. PLoS One 10,

Kim, D.H., Kshitiz, Smith, R.R., Smith, R.R., Kim, P., Ahn, E.H., Kim, H.N., Marbán, E., Suh, K.Y., and Levchenko, A. (2012). Nanopatterned cardiac cell patches promote stem cell niche formation and myocardial regeneration. Integr. Biol. 4, 1019-1033.

Kim, H.E., Dalal, S.S., Young, E., Legato, M.J., Weisfeldt, M.L., and D'Armiento, J. (2000). Disruption of the myocardial extracellular matrix leads to cardiac dysfunction. J. Clin. Invest. 106, 857-866.

Knoll, S.G., Ali, M.Y., and Saif, M.T.A. (2014). A novel method for localizing reporter fluorescent beads near the cell culture surface for traction force microscopy. J. Vis. Exp., 51873.

Kolberg, L., Raudvere, U., Kuzmin, I., Vilo, J., and Peterson, H. (2020). gprofiler2 - an R Package for Gene List Functional Enrichment Analysis and Namespace Conversion Toolset g:Profiler. F1000Res. 9.

Kolwicz, S.C., Jr., and Tian, R. (2011). Glucose metabolism and cardiac hypertrophy. Cardiovasc. Res. 90, 194-201.

Kshitiz, Afzal, J., Kim, D.H., and Levchenko, A. (2014). Concise review: mechanotransduction via p190RhoGAP regulates a switch between cardiomyogenic and endothelial lineages in adult cardiac progenitors. Stem Cell. 32, 1999-

Kshitiz, Hubbi, M.E., Ahn, E.H., Downey, J., Afzal, J., Kim, D.H., Rey, S., Chang, C., Kundu, A., Semenza, G.L., et al. (2012). Matrix rigidity controls endothelial differentiation and morphogenesis of cardiac precursors. Sci.

Kumar, N., Sridharan, D., Palaniappan, A., Dougherty, J.A., Czirok, A., Isai, D.G., Mergaye, M., Angelos, M.G., Powell, H.M., and Khan, M. (2020). Scalable biomimetic coaxial aligned nanofiber cardiac patch: a potential model for "clinical trials in a dish. Front. Bioeng. Biotechnol. 8, 567842.

Lewandowski, J., Rozwadowska, N., Kolanowski, T.J., Malcher, A., Zimna, A., Rugowska, A., Fiedorowicz, K., Łabędź, W., Kubaszewski, Ł., Chojnacka, K., et al. (2018). The impact of in vitro cell culture duration on the maturation of human cardiomyocytes derived from induced pluripotent stem cells of myogenic origin. Cell Transplant. 27, 1047-1067.

Liu, J., Laksman, Z., and Backx, P.H. (2016). The electrophysiological development of cardiomyocytes. Adv. Drug Deliv. Rev. 96, 253-273.

Liu, J., Lieu, D.K., Siu, C.W., Fu, J.D., Tse, H.F., and Li, R.A. (2009). Facilitated maturation of Ca2+ handling properties of human embryonic stem cell-derived cardiomyocytes by calsequestrin expression. Am. J. Physiol. Cell Physiol. 297, C152-C159.

Liu, Q., Tian, S., Zhao, C., Chen, X., Lei, I., Wang, Z., and Ma, P.X. (2015). Porous nanofibrous poly(L-lactic acid) scaffolds supporting cardiovascular progenitor cells for cardiac tissue engineering. Acta Biomater. 26, 105-114.

Liu, W., Acín-Peréz, R., Geghman, K.D., Manfredi, G., Lu, B., and Li, C. (2011). Pink1 regulates the oxidative phosphorylation machinery via mitochondrial fission. Proc. Natl. Acad. Sci. USA 108, 12920-12924.

Lopaschuk, G.D., and Jaswal, J.S. (2010). Energy metabolic phenotype of the cardiomyocyte during development, differentiation, and postnatal maturation. J. Cardiovasc. Pharmacol. 56, 130-140.

Lopaschuk, G.D., Ussher, J.R., Folmes, C.D.L., Jaswal, J.S., and Stanley, W.C. (2010). Myocardial fatty acid metabolism in health and disease. Physiol. Rev. 90, 207-258.

López-Acosta, O., de Los Angeles Fortis-Barrera, M., Barrios-Maya, M.A., Ramírez, A.R., Aguilar, F.J.A., and El-Hafidi, M. (2018). Reactive oxygen species from NADPH oxidase and mitochondria participate in the proliferation of aortic smooth muscle cells from a model of metabolic syndrome. Oxid. Med. Cell. Longev. 2018, 5835072.

Lundy, S.D., Zhu, W.Z., Regnier, M., and Laflamme, M.A. (2013). Structural and functional maturation of cardiomyocytes derived from human pluripotent stem cells. Stem Cells Dev. 22, 1991-2002.

Lunt, S.Y., and Vander Heiden, M.G. (2011). Aerobic glycolysis: meeting the metabolic requirements of cell proliferation. Annu. Rev. Cell Dev. Biol. 27,

Madamanchi, N.R., and Runge, M.S. (2013). Redox signaling in cardiovascular health and disease. Free Radic. Biol. Med. 61, 473-501.

Mamidi, A., Prawiro, C., Seymour, P.A., de Lichtenberg, K.H., Jackson, A., Serup, P., and Semb, H. (2018). Mechanosignalling via integrins directs fate decisions of pancreatic progenitors. Nature 564, 114-118.

Mammoto, T., and Ingber, D.E. (2010). Mechanical control of tissue and organ development. Development 137, 1407-1420.

Marian, A.J., and Braunwald, E. (2017). Hypertrophic cardiomyopathy: genetics, pathogenesis, clinical manifestations, diagnosis, and therapy. Circ. Res. 121, 749-770.

McLellan, M.A., Skelly, D.A., Dona, M.S.I., Squiers, G.T., Farrugia, G.E., Gaynor, T.L., Cohen, C.D., Pandey, R., Diep, H., Vinh, A., et al. (2020). High-resolution transcriptomic profiling of the heart during chronic stress reveals cellular drivers of cardiac fibrosis and hypertrophy. Circulation 142, 1448–1463.

Meyer, A.J., and Dick, T.P. (2010). Fluorescent protein-based redox probes. Antioxid. Redox Signal. 13, 621-650.

Paige, S.L., Plonowska, K., Xu, A., and Wu, S.M. (2015). Molecular regulation of cardiomyocyte differentiation. Circ. Res. 116, 341-353.

Passier, R., Orlova, V., and Mummery, C. (2016). Complex tissue and disease modeling using hiPSCs. Cell Stem Cell 18, 309-321.

Patra, C., Diehl, F., Ferrazzi, F., van Amerongen, M.J., Novoyatleva, T., Schaefer, L., Mühlfeld, C., Jungblut, B., and Engel, F.B. (2011). Nephronectin regulates atrioventricular canal differentiation via Bmp4-Has2 signaling in zebrafish. Development 138, 4499-4509.

Patra, C., Ricciardi, F., and Engel, F.B. (2012). The functional properties of nephronectin: an adhesion molecule for cardiac tissue engineering. Biomaterials 33, 4327-4335.

Phillips, N.R., Sprouse, M.L., and Roby, R.K. (2014). Simultaneous quantification of mitochondrial DNA copy number and deletion ratio: a multiplex realtime PCR assay. Sci. Rep. 4, 3887.

Picard, M., Taivassalo, T., Gouspillou, G., and Hepple, R.T. (2011). Mitochondria: isolation, structure and function. J. Physiol. 589, 4413–4421.

Ronaldson-Bouchard, K., Ma, S.P., Yeager, K., Chen, T., Song, L., Sirabella, D., Morikawa, K., Teles, D., Yazawa, M., and Vunjak-Novakovic, G. (2018).



Advanced maturation of human cardiac tissue grown from pluripotent stem cells. Nature 556, 239-243.

Rossi, M.A. (1998). Pathologic fibrosis and connective tissue matrix in left ventricular hypertrophy due to chronic arterial hypertension in humans. J. Hypertens. 16, 1031-1041.

Ruan, J.L., Tulloch, N.L., Razumova, M.V., Saiget, M., Muskheli, V., Pabon, L., Reinecke, H., Regnier, M., and Murry, C.E. (2016). Mechanical stress conditioning and electrical stimulation promote contractility and force maturation of induced pluripotent stem cell-derived human cardiac tissue. Circulation 134, 1557-1567.

Sabass, B., Gardel, M.L., Waterman, C.M., and Schwarz, U.S. (2008). High resolution traction force microscopy based on experimental and computational advances. Biophys. J. 94, 207-220.

Salabei, J.K., Gibb, A.A., and Hill, B.G. (2014). Comprehensive measurement of respiratory activity in permeabilized cells using extracellular flux analysis. Nat. Protoc. 9, 421-438.

Santos, C.X.C., Anilkumar, N., Zhang, M., Brewer, A.C., and Shah, A.M. (2011). Redox signaling in cardiac myocytes. Free Radic. Biol. Med. 50, 777–793.

Sartiani, L., Bettiol, E., Stillitano, F., Mugelli, A., Cerbai, E., and Jaconi, M.E. (2007). Developmental changes in cardiomyocytes differentiated from human embryonic stem cells: a molecular and electrophysiological approach. Stem Cell. 25, 1136-1144.

Schwach, V., and Passier, R. (2019). Native cardiac environment and its impact on engineering cardiac tissue. Biomater. Sci. 7, 3566-3580.

Schwer, B., and Verdin, E. (2008). Conserved metabolic regulatory functions of sirtuins. Cell Metab. 7, 104-112.

Sewanan, L.R., Schwan, J., Kluger, J., Park, J., Jacoby, D.L., Qyang, Y., and Campbell, S.G. (2019). Extracellular matrix from hypertrophic myocardium provokes impaired twitch dynamics in healthy cardiomyocytes. JACC. Basic Transl. Sci. 4. 495-505.

Shadrin, I.Y., Allen, B.W., Qian, Y., Jackman, C.P., Carlson, A.L., Juhas, M.E., and Bursac, N. (2017). Cardiopatch platform enables maturation and scale-up of human pluripotent stem cell-derived engineered heart tissues. Nat. Commun. 8, 1825.

Shi, M., Tien, N.T., de Haan, L., Louisse, J., Rietjens, I.M.C.M., and Bouwmeester, H. (2020). Evaluation of in vitro models of stem cell-derived cardiomyocytes to screen for potential cardiotoxicity of chemicals. Toxicol. Vitro 67, 104891.

Silva, A.C., Pereira, C., Fonseca, A.C.R.G., Pinto-do-Ó, P., and Nascimento, D.S. (2020). Bearing my heart: the role of extracellular matrix on cardiac development, homeostasis, and injury response. Front. Cell Dev. Biol. 8, 621644.

Slenter, D.N., Kutmon, M., Hanspers, K., Riutta, A., Windsor, J., Nunes, N., Mélius, J., Cirillo, E., Coort, S.L., Digles, D., et al. (2018). WikiPathways: a multifaceted pathway database bridging metabolomics to other omics research. Nucleic Acids Res. 46, D661-D667.

Smith, A.S.T., Yoo, H., Yi, H., Ahn, E.H., Lee, J.H., Shao, G., Nagornyak, E., Laflamme, M.A., Murry, C.E., and Kim, D.H. (2017). Micro- and nano-patterned conductive graphene-PEG hybrid scaffolds for cardiac tissue engineering. Chem. Commun. 53, 7412-7415.

Stanley, W.C., Recchia, F.A., and Lopaschuk, G.D. (2005). Myocardial substrate metabolism in the normal and failing heart. Physiol. Rev. 85, 1093–1129.

Stark, C., Breitkreutz, B.J., Reguly, T., Boucher, L., Breitkreutz, A., and Tyers, M. (2006). BioGRID: a general repository for interaction datasets. Nucleic Acids Res. 34, D535-D539.

Subramanian, A., Tamayo, P., Mootha, V.K., Mukherjee, S., Ebert, B.L., Gillette, M.A., Paulovich, A., Pomeroy, S.L., Golub, T.R., Lander, E.S., and Mesirov, J.P. (2005). Gene set enrichment analysis: a knowledge-based approach for interpreting genome-wide expression profiles. Proc. Natl. Acad. Sci. USA 102. 15545-15550.

Sung, T.C., Su, H.C., Ling, Q.D., Kumar, S.S., Chang, Y., Hsu, S.T., and Higuchi, A. (2020). Efficient differentiation of human pluripotent stem cells into cardiomyocytes on cell sorting thermoresponsive surface. Biomaterials 253,

Tanner, L.B., Goglia, A.G., Wei, M.H., Sehgal, T., Parsons, L.R., Park, J.O., White, E., Toettcher, J.E., and Rabinowitz, J.D. (2018). Four key steps control glycolytic flux in mammalian cells. Cell Syst. 7, 49-62.e8.

Thielicke, W., and Stamhuis, E.J. (2014). PIVlab -towards user-friendly, affordable and accurate digital particle image velocimetry in MATLAB. J. Open Res.

Thompson, W.R., Nadal-Ginard, B., and Mahdavi, V. (1991). A MyoD1-independent muscle-specific enhancer controls the expression of the beta-myosin heavy chain gene in skeletal and cardiac muscle cells. J. Biol. Chem. 266, 22678-22688

Tohyama, S., Hattori, F., Sano, M., Hishiki, T., Nagahata, Y., Matsuura, T., Hashimoto, H., Suzuki, T., Yamashita, H., Satoh, Y., et al. (2013). Distinct metabolic flow enables large-scale purification of mouse and human pluripotent stem cell-derived cardiomyocytes. Cell Stem Cell 12, 127-137.

Tu, C., Chao, B.S., and Wu, J.C. (2018). Strategies for improving the maturity of human induced pluripotent stem cell-derived cardiomyocytes. Circ. Res. 123,

Uosaki, H., Cahan, P., Lee, D.I., Wang, S., Miyamoto, M., Fernandez, L., Kass, D.A., and Kwon, C. (2015). Transcriptional landscape of cardiomyocyte maturation. Cell Rep. 13, 1705-1716.

Vining, K.H., and Mooney, D.J. (2017). Mechanical forces direct stem cell behaviour in development and regeneration. Nat. Rev. Mol. Cell Biol. 18, 728-742.

Wang, Y.L., and Pelham, R.J., Jr. (1998). Preparation of a flexible, porous polyacrylamide substrate for mechanical studies of cultured cells. Methods Enzymol. 298, 489-496.

Weinberger, F., Mannhardt, I., and Eschenhagen, T. (2017). Engineering cardiac muscle tissue: a maturating field of research. Circ. Res. 120, 1487-1500.

Wixon, J., and Kell, D. (2000). The Kyoto encyclopedia of genes and genomes-KEGG. Yeast 17, 48-55.

Wrighton, P.J., Klim, J.R., Hernandez, B.A., Koonce, C.H., Kamp, T.J., and Kiessling, L.L. (2014). Signals from the surface modulate differentiation of human pluripotent stem cells through glycosaminoglycans and integrins. Proc. Natl. Acad. Sci. USA 111, 18126-18131.

Yang, X., Pabon, L., and Murry, C.E. (2014). Engineering adolescence: maturation of human pluripotent stem cell-derived cardiomyocytes. Circ. Res.

Yu, J., Lee, A.R., Lin, W.H., Lin, C.W., Wu, Y.K., and Tsai, W.B. (2014). Electrospun PLGA fibers incorporated with functionalized biomolecules for cardiac tissue engineering. Tissue Eng. Part A 20, 1896-1907.

Zhao, X., Cai, A., Peng, Z., Liang, W., Xi, H., Li, P., Chen, G., Yu, J., and Chen, L. (2019). JS-K induces reactive oxygen species-dependent anti-cancer effects by targeting mitochondria respiratory chain complexes in gastric cancer. J. Cell Mol. Med. 23, 2489-2504.





STAR***METHODS**

KEY RESOURCES TABLE

REAGENT or RESOURCE	SOURCE	IDENTIFIER
Antibodies		
Goat Anti-Rabbit IgG (H+L) Antibody, Alexa Fluor 568 Conjugated	Thermo Fisher Scientific	Cat# A-11011, RRID: AB_143157
Goat anti-Mouse IgG (H+L) Highly Cross-Adsorbed Secondary Antibody, Alexa Fluor Plus 488	Thermo Fisher Scientific	Cat# A32723, RRID: AB_2633275
Goat anti-Rabbit IgG (H+L) Highly Cross-Adsorbed Gecondary Antibody, Alexa Fluor Plus 488	Thermo Fisher Scientific	Cat# A32731, RRID: AB_2633280
Goat anti-Mouse IgG (H+L) Cross-Adsorbed Secondary Antibody, Alexa Fluor 568	Thermo Fisher Scientific	Cat# A-11004, RRID: AB_2534072
Alexa Fluor 594 Phalloidin antibody	Thermo Fisher Scientific	Cat# A12381, RRID: AB_2315633
Connexin 43 antibody	Thermo Fisher Scientific	Cat# 35-5000, RRID: AB_2533207
Sarcomeric alpha Actinin antibody	Thermo Fisher Scientific	Cat# MA1-22863, RRID: AB_557426
Cardiac Troponin T antibody	Thermo Fisher Scientific	Cat# MA5-12960, RRID: AB_11000742
Cardiac Troponin I antibody	Abcam	Cat# ab47003, RRID: AB_869982
Myosin Light Chain 2 antibody	Abcam	Cat# ab79935, RRID: AB_1952220
Wheat Germ Agglutinin, Alexa Fluor [™] 488 Conjugate	Thermo Fisher Scientific	Cat# W11261
PDK1 (D37A7) Rabbit mAb antibody	Cell Signaling Technology	Cat# 5662, RRID: AB_10839264
AceCS1 (D19C6) XP(tm) Rabbit mAb antibody	Cell Signaling Technology	Cat# 3658, RRID: AB_2222710
Fatty Acid Synthase (C20G5) Rabbit mAb antibody	Cell Signaling Technology	Cat# 3180, RRID: AB_2100796
PFKP antibody	Cell Signaling Technology	Cat# 12746, RRID: AB_2736917
Fotal OXPHOS Rodent WB Antibody Cocktail	Abcam	Cat# ab110413, RRID: AB_2629281
Donkey Anti-Rabbit IgG ECL Antibody, HRP Conjugated	GE Healthcare	Cat# NA9340-1 ml, RRID: AB_772191
Sheep Anti-Mouse IgG ECL Antibody, HRP Conjugated	GE Healthcare	Cat# NA9310-1 ml, RRID: AB_772193
Chemicals, peptides, and recombinant proteins		
GRGDS	Peptides International	PFA-4189-v
GFPGER	Sigma-Aldrich	165044K
Nephronectin	Novus Biologicals	9560-NP-050
Endothelin 1	Sigma-Aldrich	E7764
CHIR99021	LC Laboratories	C-6556
WR-1	Selleck Chemicals	S7086
SYLGARD 184	Sigma-Aldrich	761028
oligomycin	Sigma-Aldrich	O4876
Rotenone	Sigma-Aldrich	R8875
Antimycin A	Sigma-Aldrich	A8674
Carbonyl cyanide 4-(trifluoromethoxy)phenylhydrazone	Sigma-Aldrich	C2920
Deposited data		
RNA sequencing (RNA-seq)	This manuscript	GSE134845
Oligonucleotides		
mtND1 FP: CTAAATAGCCCACACGTTCCC	Phillips et al., 2014	N/A
mtND1 RP: AGAGCTCCCGTGAGTGGTT	Phillips et al., 2014	N/A
mtND1 Probe: CATCACGATGGATCACAGGT	Phillips et al., 2014	N/A
mtND4 FP: CTGTTCCCCAACCTTTTCCT	Phillips et al., 2014	N/A
mtND4 RP: CCATGATTGTGAGGGGTAGG	Phillips et al., 2014	N/A
mtND4 Probe: GACCCCTAACAACCCCC	Phillips et al., 2014	N/A
	Phillips et al., 2014 Phillips et al., 2014	N/A N/A

(Continued on next page)



Continued		
REAGENT or RESOURCE	SOURCE	IDENTIFIER
B2M Probe: CAGCAGCCTATTCTGC	Phillips et al., 2014	N/A
Recombinant DNA		
pGP-CMV-GCaMP6f	Addgene	Plasmid #40755
ArcLight	Addgene	Plasmid #36857
CMV-VARNAM	Addgene	Plasmid #115552
pLEX_307	Addgene	plasmid # 41392
pLPCX cyto Grx1-roGFP2	Addgene	Plasmid #64975
Software and algorithms		
R	Opensource	www.R-project.org

RESOURCE AVAILABILITY

Lead contact

Further information and requests for resources and reagents should be directed to and will be fulfilled by the lead contact, Kshitiz (kshitiz@uchc.edu).

Materials availability

Substrates generated in this study can be available from lead contact with a completed Materials Transfer Agreement (MTA).

Data and code availability

- RNA-seg data generated in this study has been deposited in NCBI's GeneExpression Omnibus (GEO) with the accession number GEO: GSE134845. Human data for comparative studies was obtained from NCBI GEO with following accession numbers: GEO: GSM2343070, GEO: GSM1698563, and GEO: GSM1698564.
- All the original codes for Steiner tree-based Protein-Protein Interaction Map analysis are on Github (https://github.com/yasirs/ cardiac-maturation-submission), and the Zenodo code is listed in key resources table.
- Any additional information required to reanalyze the data reported in this paper is available from the lead contact upon request.

METHOD DETAILS

Human iPSC culture and cardiac differentiation

Human iPSCs (WTC-11, HF-YK27 and PBY4-48D) were cultured using chemically defined medium and published protocols (Burridge et al., 2014; Tohyama et al., 2013). WTC-11 was primarily used in the study, and HF-YK27 and PBY4-48D were used to test the effect of CMM on multiple iPSCs lines (Figure S7). Undifferentiated iPSCs were seeded (125,000 cells per cm2) on Geltrex (ThermoScientific)-coated six-well plates and maintained in E8 medium (Life Technologies) for 4 days when they reached 80-85% confluence. Medium was then changed to cardiac differentiation medium (CDM), consisting of RPMI 1640 medium (11875, ThermoScientific), 500 μg/ml O. sativa-derived recombinant human albumin (A9731, Sigma-Aldrich), and 220 μg/ml L-ascorbic acid (A4544-Sigma-Aldrich), containing B27 supplement-insulin free (A1895601 ThermoScientific) to initiate differentiation. On d0-d2, medium was supplemented with 6 μM CHIR99021 (LC Laboratories) for induction of mesoderm. On d4-d5, medium was supplemented with 10uM IWR (Selleck Chemicals) for cardiac differentiation. Contracting cells are typically noted, starting on d7-d8. To purify cardiac myocytes, a variant of RPMI 1640 medium without D-glucose (11879, Life Technologies) was supplemented with 4 mM sodium lactate (L4263, Sigma-Aldrich) for 2 days on day10 of differentiation followed by culture in cardiac media, containing B-27TM Supplement with insulin (17504001, ThermoScientific) in CDM medium (Tohyama et al., 2013). Cells were dissociated on d13-d14 using TrypLE (ThermoScientific) and plated/cultured on either flat/anisotropic cell culture surfaces for 15-16 further days (d30 for flat and CMM) or 45 days (d60 for flat culture surface) in cardiac culture media. Cardiac culture media was used in all the conditions from day13-d14 onwards, and it was composed of RPMI-1640, lipid-enhanced Cellastium S, 220 µg/ml L-ascorbic acid and B27 with insulin. Control flat tissue-culture surfaces were coated with fibronectin at a concentration of 4 μg/cm². For hypertrophy induction, day 30 differentiated cells were treated with 10 nM endothelin 1 (E7764 Millipore Sigma) for 48hrs in cardiac culture media.

Fabrication of nanowrinkled molds for cardiac mimetic matrix

Polydimethylsiloxane (PDMS) was prepared by mixing the pre-polymer and curing agent in a 10:1 ratio (Dow Corning Sylgard 184), cured at RT or 24 h on a horizontal surface followed by thermal curing of 4 h at 65°C. PDMS slabs (4 (L) × 2 (W) x 0.3 (H) cm) were then uniaxially stretched to yield 30% strain using a home-made mechanical stretcher and plasma treated with a plasma cleaner (Harrick Plasma PDC32G) with medium RF power for 5 min. PDMS nanowrinkles were obtained upon releasing the PDMS slabs from the





mechanical stretcher. A library of PDMS nanowrinkles with various periodicity and depth can be achieved by modulating the strain, RF power, and plasma treatment time. The nanowrinkled slab was then transferred to a polyurethane (PU) mold by replica molding. This was achieved by drop dispensing 100 μ L PU prepolymer (NOA 76) onto a clean glass slide and covering the drop with PDMS slab and placing a 3-gram weight on the slab for 5 min. Cross-link NOA76 with a UV Cross linker (UV Stratalinker 188; 365 nm) for 20 min. Cool the sample at room temperature before peeling off the PDMS mold. SEM images of PDMS and PU molds were obtained using a Hitachi TM1000 tabletop SEM.

Fabrication of cardiac mimetic matrix substrates

PU molds, bonded to PET sheets for ease of handling, were used as a replica mold to transfer polyacrylamide (PA) topographic patterns. PEG with a similar elasticity was also tested, and we found no difference between either PEG or PA as measured by calcium response to caffeine, or RT-PCR of a panel of cardiac genes. PA precursor was prepared by mixing 10% acrylamide and 0.225% bisacrylamide solution to yield an expected 23 kPa gel. After degassing for 30 min, 0.05% v/v tetramethylethylenediamine (TEMED) and 0.5% v/v 10% ammonium persulphate (APS) was mixed with precursor solution by gently pipetting. Precursor solution was dispersed onto PU mold and covered with salinized coverslip for 20 min in a wet chamber. After cross-linking the hydrogel was immersed in 1x PBS for 1 h before peeling off from PU mold. All the samples were stored in 1x PBS solution at 4°C. AFM imaging of the surface topography of the hydrogel was performed using Asylum Research Cypher AFM with a PNP-TR probe in 1x PBS.

Functionalization of CMM and Raman spectroscopy

Samples were functionalized with 1.3 mg/mL Sulfo-SANPAH under UV for 10 min and incubated in GRGDS (Peptides International PFA-4189-v), GFPGER (Sigma-Aldrich 165044K), and nephronectin (Novus 9560-NP-050) solutions at 4° C overnight. The samples were washed with 1x PBS for 3 times and stored in PBS at 4° C before Raman spectroscopy or cell culture. Raman spectroscopy of functionalized hydrogel was performed using WITec alpha300 R Raman microscopy with a $40\times$ immersive objective in 1x PBS using a 785 nm laser. Briefly, five kinds of samples were prepared: hydrogel functionalized with (i) no ligands, (ii) GRGDS, (iii) GFPGER, (iv) nephronectin, and (v) GRGDS/GFPGER/nephronectin. Individual spectrums of samples (i)-(iv) were obtained with integration time of 1 s and accumulation of 60 times. Distribution of each component in sample (v) was obtained by true component analysis of the largearea Raman scan (50 μ m \times 50 μ m, with resolution of 50 pixel \times 50 pixel) based on the individual spectrums of samples (i)-(iv). Raman spectroscopic xy scan in Figure 1H shows the percentage of each ligand in the legend.

RT-PCR

Cells were harvested, and RNA was isolated using RNeasy Mini Kit (Qiagen). cDNA was synthesized using SuperScript VILO Master Mix (ThermoScientific). Taqman predesigned assays (ThermoScientific) were used to perform qRT-PCR on CFX384 Touch Real-Time PCR Detection System (Biorad). The assays ids are: KCNJ2 (Hs01876357_s1), CASQ2 (Hs00154286_m1), CAMK2D (Hs00943538_m1), TTN (Hs00399225_m1), MYL2 (Hs00166405_m1), PFKM (Hs01075411_m1), PDHB (Hs00168650_m1), LDH (Hs00855332_g1), HK2 (Hs00606086_m1), HK1(Hs00175976_m1), NOS1 (Hs00167223_m1), TXN (Hs01555214_g1), MYBPC2 (Hs00189825_m1), CAV3 (Hs00154292_m1), MYOM1 (Hs00187003_m1), and the transcripts were normalized to endogenous GAPDH Control (VIC / MGB Probe, Primer Limited, 4326317E).

In Figure 2H, Black dot (comparison of anisotropic nanowrinkles (ANW) or d30 + matrix with d30), blue dot (comparison of CMM with ANW), red dot (comparison of CMM with d30 + matrix). Ligands is flat surface coated with matrix, CMM without matrix is nanopatterned platform without matrix, CMM is matrix coated Nano surface. Error bars show standard deviation; d30 is control condition. In Figure 2I, other anisotropic surfaces: Plga-AES (poly(lactide-co-glycolide) aligned electrospun nanofibers), PU-CFL (polyurethane-capillary force lithography). Same batch of cells were plated on same day (d11) on difference surfaces and lysed on d30 for relative gene quantification with Tukey's multi comparison with adjusted p value (in Figure S8).

Mitochondrial number

Mitochondrial number was quantified by estimating the amount of mitochondrial DNA (mt-ND1 & mt-ND4) relative to nuclear DNA (B2M) using probe-based Taqman Real-Time PCR as described earlier (primer/probes sequence and concentration) (Phillips et al., 2014).

mtND1 FP: CTAAATAGCCCACACGTTCCC.

RP: AGAGCTCCCGTGAGTGGTT, Probe: CATCACGATGGATCACAGGT.

mtND4 FP: CTGTTCCCCAACCTTTTCCT.

RP: CCATGATTGTGAGGGGTAGG, Probe: GACCCCCTAACAACCCCC.

B2M FP: GCTGGGTAGCTCTAAACAATGTATTCA,

RP: CCATGTACTAACAAATGTCTAAAATGGT, Probe: CAGCAGCCTATTCTGC

RNA sequencing and analysis

RNA was isolated using RNeasy Mini Kit (Qiagen). Bioanalyzer 2100 (Agilent) was used to check the RNA integrity and samples with RIN <8 were used for library preparation. Library preparation and RNA sequencing were performed by Yale Center for Genome Analysis (YCGA). Reads were aligned to the NCBI GRCh38 genome assembly using the HISAT2 pipeline with default parameters. Reads

Cell Reports Article



were counted using HTSeq. Fold changes and statistical significance (p values) for differential expression were calculated using DE-Seq2. p-values for differential expression were calculated for the Wald test.

For each functional category the following gene sets were used from the Gene Ontology (Harris et al., 2004), KEGG (Wixon and Kell, 2000), Msigdb (Subramanian et al., 2005), WikiPathways (Slenter et al., 2018), and EBI (Huntley et al., 2015) were used to select the genes to include in the transcriptomic analysis.

Functional category	Gene sets included	Source
Metabolism Figure 5A)	Gluconeogenesis (KEGG)	MSigDB
	Cell Redox Homeostasis (GO)	MSigDB
	Genes involved in Oxidative Phosphorylation(Pubmed 12808457)	MSigDB
	Fatty Acid Catabolic Process (GO)	MSigDB
Calcium handling and contractility (Figure 5B)	Calcium Regulation in the Cardiac cell (http://www.ncbi.nlm.nih.gov/pubmed/12618512)	WikiPathways
	Regulation of Cardiac Muscle Contraction by Calcium Ion Signaling (GO)	MSigDB
Voltage and Action (Figure 5C)	Action Potential (GO)	MSigDB
Structure (Figures 3A and 3B)	Regulation of Actin Cytoskeleton (KEGG)	MSigDB
	Focal Adhesion (KEGG)	MSigDB
	ECM Receptor Interaction (KEGG)	MSigDB
	Gap Junction (KEGG)	MSigDB
Mechanics	Myosin II Complex (GO)	MSigDB
	Sarcomere Organization (GO)	MSigDB
	Titin Binding (GO)	MSigDB
	Actinin Binding (G)	MSigDB
Cardiac Cell Development (Figures 2D and 2F)	Cardiac Cell Development (GO)	MSigDB
Cardiac muscle cell differentiation (Figure 7)	Cardiac muscle cell differentiation (GO)	EBI
Actomyosin Organization (Figure 7)	Actomyosin Organization (GO)	EBI
Mitochondrial Fusion (Figure 3O)	Mitochondrial Fusion (GO)	EBI

Hierarchical clustering using UPGMA method with eucledian distance were performed on samples and z-scores of all differentially regulated genes in either condition, sorted using Anova analysis with FDR correction of 0.05) and 9 main clusters were observed. Ontologies were evaluated in each cluster in GO, Wikipathways, Kegg and Reactome using gprofiler2 (Kolberg et al., 2020).

In hive plots (Figures 2A, 2B and 3A), the position of each gene is along an axis is dependent on the Z score for that condition. Genes that are up-regulated (down-regulated) in the direction of maturation are linked by brown (green) curves (brown: positive, green: negative z-scores); Curves are brown if expression increases, and green if expression decreases in the direction of systemic maturation. Arrows refer to the direction of maturation. 30 days cells (d30) were picked as controls. In using Ingenuity Pathway Analysis (IPA) analysis (Figure 2C), size of circles represents the magnitude of the activation score vs d30, and color represent activation Z score calculated based on changes in the expression of known targets of given TFs. In Figure 7C of IPA analysis, size of circles represents the p value overlap with the given set of targets.

Immunostaining

Cultured cells were washed twice with PBS before fixing them with 4% paraformaldehyde (pH 7.4) for 15 min at room temperature. After fixation, cells were washed with cold PBS before permeabilizing them with PBS buffer containing 0.2% Triton X-100 and 0.1% BSA for 15 min followed by one-hour incubation with blocking buffer (1% BSA in PBS). Cells were then incubated overnight with primary antibodies with subsequent 30 min incubation with secondary antibody. Following primary antibodies were used for labeling; Alexa Fluor 594 phalloidin (ThermoFisher A12381), Connexin 43 (ThermoFisher 35-5000), sarcomeric alpha actinin (ThermoFisher MA1-22863), cardiac troponin T (ThermoFisher MA5-12960), cardiac troponin I (Abcam ab47003), MYL2 (Abcam ab79935), and Wheat Germ Agglutinin, Alexa Fluor 488 Conjugate (ThermoFisher W11261). Following Alexa Fluor Secondary Antibodies (ThermoFisher) were used: Alexa Fluor 568 (A-11004, A-11011), Alexa Fluor 488 (A32723, A32731). Cells were counterstained with DAPI (ThermoFisher D21490) before imaging. The data was analyzed using ImageJ software (version 1.48, National Institutes of Health, Bethesda, MD, USA).





Confocal and airyscan imaging

Confocal Images were acquired using a laser scanning confocal microscope, Zeiss LSM 880. Images were taken using a 63x oil objective. Imaging was performed on LSM 880 laser scanning confocal microscope (ZEISS) equipped with 63X Plan Apochromatic 1.40 NA oil objective, an Airyscan super-resolution module, GaAsP detectors and Zen Black acquisition software (ZEISS). The pixel dwell time, laser intensity and detector gain were kept low to avoid saturation and photobleaching during the image acquisition. To increase signal-to-noise ratio and resolution, acquired images were processed by 3D Airyscan filter strength 7.0 with Zen Black software.

Imaging in Figure 3N and Data S1 is with pixel size 0.041X0.041 μm, image size of 202X202 μm and 9 Tiles.

Imaging in Figures S10A and S10B is with pixel size 0.070X0.070 μm, image size of 133 X133 μm and 9 Tiles.

Imaging in Figure S9A is with pixel size 0.070X0.070 μm, image size of 268 X133 μm and 8 Tiles.

Banding patterns prevalent as signatures of cardiac maturity were measured using ImageJ and analyzed using custom MATLAB scripts. Banding frequency was measured as the spatial metric between peak intensities of myosin light chain in the respective a-Actinin and cardiac troponin (cTnT) images.

Flow cytometry

Cells were detached from the substrate with TrypLE (Gibco), quenched with excess medium, and washed thrice with phosphatebuffered saline (PBS). Isolated cells were either labeled with the requisite dye (Mitotracker-Green at 100 nM for 15 min, and washed twice with PBS), or fixed in 4% paraformaldehyde in PBS and stained with primary and secondary antibodies with method described previously (Hubbi et al., 2013; Kshitiz et al., 2012). Primary antibodies used were: Myosin Light Chain 2 (Abcam ab79935), sarcomeric alpha actinin (ThermoFisher MA1-22863) and cardiac troponin T (ThermoFisher MA5-12960). Cells were analyzed in a BD FacsARIA II, and analyzed using Flowing software (Turku University). Gating was performed using the requisite negative controls in each channel with unlabeled cells.

Immunoblots

Three different biological replicates (batches) were generated using separate cultures/cardiac differentiations of iPSCs for immunoblots. Samples were harvested and lysed in buffer containing radioimmunoprecipitation assay lysis buffer (Cell Signaling Technology 9806), protease inhibitors (Sigma-Aldrich P8340) and phosphatase inhibitors (Sigma-Aldrich 4906845001-PhosSTOP). Protein concentration was quantified using bicinchoninic acid assay kit (Thermo Fisher Scientific). Proteins were denatured 95°C for 5 min in SDS and 20 µg of samples were loaded on 4-12% NuPAGE Bis-Tris Gel (Thermo Fisher Scientific NP0322BOX). They were transferred to polyvinylidene difluoride (PVDF) membranes, and subsequently blocked with 5% BSA for 1 h at room temperature and incubated overnight at 4°C with primary antibody —cardiac troponin I (Abcam ab47003); Troponin T (ThermoFisher MA5-12960), PDK1 (Cell Signaling Technology 5662), AceCS1 (Cell Signaling Technology 3658), FAS (Cell Signaling Technology 3180), PFPK (Cell Signaling Technology 12746). For Total OxPhos primary antibody (Abcam ab110413), samples were prepared in lysis buffer (as above) but loaded onto the gel without denaturation. Proteins samples were transferred onto PVDF membranes at 4°C and equal protein loading was verified with Ponceau S staining solution (Cell Signaling Solution 59803). Following the primary antibody incubation, membranes were washed several times before incubation with GAPDH (Cell Signaling Technology 5174) for 1 h at room temperature. Subsequently, samples were incubated with horseradish peroxidase-linked anti-rabbit or mouse IgG secondary antibody (GE healthcare NA9340 or NA9310) for 1 h at room temperature. An enhanced chemiluminescence reagent (Thermo Fisher Scientific 34095) was used to visualize the bands. Semi-quantification of protein was conducted by comparison against the GAPDH bands using ImageJ software.

Mitochondrial respiration

Cellular energetics was monitored using the Seahorse Bioscience XF instrument in intact cells (non-permeabilized cells) and permeabilized cells (Afzal et al., 2017; Salabei et al., 2014). Intact cell respiration was monitored to evaluate the contribution of oxidative phosphorylation versus glycolysis, whereas permeabilized cell respiration was used to monitor electron transport chain (ETC) complex function/activity using ETC complex specific substrates and fatty acid oxidation.

Respiratory rates were measured as basal rates (in the absence of added compounds/ metabolic inhibitors) and after injection of compounds through injection ports of Seahorse XF analyzer during the assay run. Specific components of ETC or glycolysis (in intact cells) were inhibited to investigate components of metabolism. We used oligomycin (4μ M) to inhibit mitochondrial F_1F_0 -ATP synthase, rotenone (2μM) to inhibit Complex 1 of ETC, antimycin A (2μM) to inhibit complex 3 of ETC, FCCP (2μM) to uncouple mitochondria for quantification of maximum respiratory capacity and iodoacetate (100μM) to inhibit glycolysis (glyceraldehyde-3phosphate dehydrogenase). The compounds were prepared as stock solutions and dissolved in the assay media immediately before the experiment. For intact cell respiration, Seahorse XF Base Medium (Part # 102353-100) with addition of D-glucose (11 mM) and glutamine (2 mM) were used.

For permeabilized cell respiration, iPSC-CMs were permeabilized using 2 nM of Seahorse XF Plasma Membrane Permeabilizer (Part #102504-100). In permeabilized cells only OCR is measured. Mitochondrial respiration was assayed using Buffer (pH 7.2) containing 137 mM KCl, 2 mM KH2PO4, 0.5 mM EGTA, 2.4 mM MgCl2, 20 mM HEPES with 0.2% fatty acid-free BSA (Sigma). Respiration rates were normalized to the protein concentration using BCA assay. Complex I respiration were evaluated by 5 mM glutamate

Cell Reports Article



and 5 mM malate (G/M) to evaluate State 4 respiration; 4 mM ADP was then injected to evaluate State 3 respiration. Maximal respiratory capacity (uncoupled mitochondria) was measured by injecting 2µM FCCP. Coupling of Electron Transport Chain respiration to ATP synthesis were evaluated using the ATP synthase inhibitor oligomycin (4uM). Complex II respiration were measured using 5 mM succinate. Fatty acid oxidation was measured by injecting 200uM of Palmitoyl-I-carnitine chloride/2.5 mM Malate and assessing the increase in OCR.

Particle image velocimetry (PIV) analysis

Time lapse movies of three given conditions were taken using a 4x magnification lens to capture the contraction dynamics over a 2.2 x 1.5 mm field of view (FOV). The images were taken using the EVOSTM Imaging system with a camera (X) equipped for image acquisition at video rate (60 Hz) over a period of 20 s. We employed particle image velocimetry metrics to track the dynamical movements of cell monolayers during the period of contraction. From the time-lapse images, the local contrast was sufficient to track movement of the monolayers over the 140x140um interrogation window. Further spatial and temporal filtering was employed to assess correct measurement of particle velocities (Thielicke and Stamhuis, 2014). We used these metrics to assess the instantaneous velocities of the monolayer over the field of view and the beating frequency. Furthermore, metrics over localized areas were used to measure the temporal signatures in the contractile moments and the directional movement of the monolayer during contraction.

Transmission Electron Microscopy

Transmission Electron Microscopy was performed by Dr. Maya Yankova at the UConn Health Central Electron Microscopy Facility. To assess the subcellular organizational changes of cardiomyocytes cultures for the two varying topographies, samples were prepared for Transmission Electron Microscopy using standard protocols. Briefly, post culturing cells in flat and CMM, samples were fixed in 2%/2.5% paraformaldyhyde/glutaraldehyde solution overnight. Following fixation, samples were treated with 1% osmium tetroxide and embedded in Epon resin for sectioning. Thin, 70 nm sections were imaged using X imaging setup at various locations using Hitachi H-7650 EM. Organelle structures such as mitochondria size and fusion, sarcomeric structures and banding were visually assessed and imaged.

Traction Force Microscopy

Polyacrylamide substrates were prepared and functionalized to measure traction forces generated by cardiomyocytes from standard gel preparation protocols (Aratyn-Schaus et al., 2010; Fischer et al., 2012; Wang and Pelham, 1998). Briefly, coverslips for gel attachment were cleaned with ethanol and sonication, treated with air plasma, and silane-activated with 0.5% glutaraldehyde and 0.5% (3-Aminopropyl)triethoxysilane. Coverslips (for TFM) and nanopatterned poly(urethane acrylate) molds (for nanoTFM) for beads coating were treated with air plasma, coated with 0.01% poly-L-lysine (PLL), and then coated with carboxylate-modified fluorescent microspheres (0.2 um; Thermo Fisher). Gel precursor solution containing 7.5% acrylamide and 0.15% bis-acrylamide was degassed for 30 min and mixed with 0.1% tetramethylethylenediamine and 0.1% ammonium persulfate before sandwiched between silaneactivated coverslips and beads-coated coverslips or molds for 20 min. Gels were functionalized using 1 mg/mL sufloSANPAH (ThermoFisher) for 10 min under UV lamp (UV StratAligner 1800) and incubated in 30ug/ml collagen type I (Thermo Fisher) overnight at 4°C. Gels were sterilized under UV for at least 2 h before cell seeding. Harvested cardiomyocytes from flat and nano substrates were seeded on functionalized gels and incubated for 36 h prior to imaging. Differential Interference Contrast (DIC) and fluorescent beads were imaged using a Zeiss Observer Z1. Monolayer contractions were imaged over a period of 20 s to accurately assess contraction dynamics of at least 4-6 cell cycles. Cells were paced at different rates by coverslips with cells in a chamber connected to grass stimulator with 4.0 ms pulse duration and 5V of current at which one to one pacing was observed at different pacing rates. Cells were then detached by trypsinization, and stress-free reference images were recorded. Traction stress calculations were performed by comparing images containing beads position displaced by cellular traction force and reference images using particle image velocimetry as described in detail (Sabass et al., 2008). Strain energy calculations were made as mentioned earlier to assess contractile energies of cardiomyocytes (Sabass et al., 2008).

Cyto-calcium, action potential and redox handling

We monitored cytoplasmic calcium and redox status of iPSC-CMs using spinning disk confocal microscope (Olympus/Andor Revolution XD). We generated 3rd gen. lentiviral probes using ViraPowerTM Lentiviral mix and transduced iPSC-CMs using MOI 5 (multiplicity of infection) that generated good signal to noise ratio. Cytoplasmic targeted roGFP-Grx1 probes (Gutscher et al., 2008), Calcium probe (genetically encoded Ca²⁺ indicators (GECIs) - GCamP6f (Chen et al., 2013), Arclight (Jin et al., 2012) and Varnam (Kannan et al., 2018) were obtained from Addgene and transferred to pENTRTM/SD/D-TOPO® vector using PCR. The vector was sequence verified and then transferred to pLEX_307 vector (Addgene plasmid # 41392) that contains the EF1α promoter using the LR reaction. The vector was sequence verified and transferred to pLEX_307 vector using the LR reaction. The virus was generated for each probe in HEK293-FT cells using an optimized mix of three packaging plasmids (pLP1, pLP2, and pLP/VSVG). The virus was concentrated using PEG-itTM Virus Precipitation Solution (SBI biosciences) that also removes HEK293-FT cell medium. MOI was calculated using qRT-PCR and MOI=5 was found to be optimal for these probes in iPSCs-CMs.

To monitor the florescence signal from cells transduced with probes, cells were plated at a density of 200,000 per cm² on cultured surfaces for at least 10-15 days prior to imaging, to achieve cell-cell coupling. During the experiment, continuous perfusion of



modified Tyrode solution was performed at 37C with pH 7.4 containing (in mM) 130 NaCl, 5 KCl, 1 MgCl₂, 2 CaCl₂, 20 Na-HEPES, 11 glucose, 2 pyruvate, 0.1% fatty acid free-BSA.

Florescence from cells (transduced with probes) was collected separately at a frame rate of 5112X512 using an electron-multiplying charge-coupled device (EMCCD) camera using Andor Revolution X1 Spinning Disk confocal inverted microscope. Data was acquired with 2X2 pixel binning. ROS (roGFP2-Grx) probes were excited with 405 nm and 488 nm laser and emission was detected using bandpass filter of 500nm-554 nm. The image 405 nm image was divided by 488 nm image (pixel by pixel), and the values are reported as the ratio of 405/488. Recovery of glutathione pool was monitored for 180-240sec before the utilization of diamide (oxidized) and DTT (reduced) to obtain min and max signal. Recovery time point of 60 s were selected as the signal was stable 60 s in most cells. Cells transduced with cytoplasmic GCamp6f were excited at 488 nm and emission was detected using bandpass filter of 500nm-554 nm. Cells transduced with Arclight were excited at 488 nm and emission was collected using bandpass filter of 500nm-554 nm. The data was analyzed using ImageJ (NIH).

To investigate calcium content of the sarcoplasmic reticulum (SR), Fura2 (ThermoFisher 3uM) loaded cells were perfused with caffeine. Cells were initially perfused with modified Tyrode solution at 37C (pH 7.4) containing (in mM) 130 NaCl, 5 KCl, 1 MgCl2, 1.2 CaCl2, 20 Na-HEPES, 10 glucose, 1 pyruvate, 0.1% fatty acid free-BSA. After pacing the cells at 0.5 Hz for 30-40 sec, cells were perfused with the modified Tyrode buffer containing caffeine (10 mM). Images were analyzed using ImageJ (NIH). Line plots (trace plots) were generated for both action potential and calcium transients by calculating average intensity (and standard deviation) from 3 biological batches with >100 cells for each time point and plotting it against the time (using R).

Steiner tree based protein-protein interaction map

We derive networks intending to generate hypotheses for proteins mediating the transcriptomic response related to specific ontologies from the ECM coated nanofabricated substrate. Our method prioritizes including the genes from a particular gene set that are differentially up-regulated in the nanofabricated structures and the ECM receptors (integrins) that are supposed to cause the response.

The networks are generated from the protein-protein interactions taken from BioGRID. In order to get the gene set related subnetwork of differentially expressed genes, we modify the Prize Collecting Steiner Tree algorithm. The prize for including a differentially regulated gene that is a member of the gene set under consideration is set as

$$p_g = \alpha (1 + f_g I_{f_g > 0}),$$

where f_i is the log2 fold change of the gene i, $I_{f_0>0}$ is the indicator function (i.e., $I_{f_0>0}=1$ if $I_0>0$, and 0 otherwise). The prize for an integrin whose ligand was coated on the substrate is β . The prize for all genes other than the ones in the gene set of interest or the receptors of interest are zero. Thus, they may be included in the network if they are needed to connect the selected integrins and upregulated genes. The edges have costs associated with them that are related to the degree and differential expression of the nodes they connect. First, the degree of each gene i in the un-wieghted validated protein-protein interaction network from BioGRID is calculated as

$$k_i = \sum_j e_{i,j}$$

Then, the cost of each edge (i,j) is set as

$$c_{i,j} = \sqrt{\frac{k_i}{1 + I_{f_i > 0}} \frac{k_j}{1 + I_{f_j > 0}}}$$

where $I_{t>0}$ is again the indicator function. The numerator is the equivalent of symmetrical degree normalization of the adjacency matrix, while the denominator has the effect of decreasing the cost for edges that connect up-regulated edges. Overall, we are penalizing promiscuous and non up-regulated genes. We use the indicator function so that we don't per se penalize down-regulation because down-regulation may either mean the shutting down of a signaling pathway or the participation of a particular gene in some complex dynamics.

The Prize Collecting Steiner Tree algorithm then attempts to join the genes with prizes using edges and any other out of set genes as needed to maximize the total gene prizes minus the total edge costs. A small set of genes needed to connect the gene set will be included by the algorithm, prioritized by their up-regulation and specificity (i.e., low degree in the PPI network). OmicsIntegrator2 was used to arrive at a solution to the optimization problem (Kedaigle and Fraenkel, 2018).

In Figure 2D, the network is generated by prioritizing up-regulated genes and non-promiscuous connections to connect the adult heart specific integrins and actomyosin organization genes to cardiac development genes using a customized Prize Collecting Steiner Tree (PCST). Edges are color coded with the cost of PCST and nodes are color coded with log fold change (lfc) of differential genes in CMM vs d30 cells. In Figure 2E, the genes included in the paths starting from each source (integrins or actomyosin organization) are shown in green in the respective column. In Figure 2F, different lines are for the genes predicted to be activated by integrins, actomyosin organization genes, both activations (Both), or by either (Total). All analysis performed on the PCST constructed using the multivalidated PPIs.

Cell Reports Article



For Figure 2D, all experimentally observed physical interactions were considered in building the Steiner Tree, while for Figures 2E-2G, the Steiner Tree was constructed using only those genes marked as multi-validated according to BioGRID based on its confirmation in multiple studies or experimental systems.

Patch clamp electrophysiology

Cardiac cells differentiated on flat and CMM substrate (d30 and CMM cells) were harvested as single cell and plated on fibronectin coated cover slips followed by few days of culture in cardiac media to recover them before performing patch clamp and action potential recording. Action potential was recorded under whole-cell current clamp mode using an Axon Axopatch 200B amplifier and pclamp9 software (Molecular Devices, USA) at room temperature. Patch pipettes were pulled from borosilicate glass tubes to give a resistance about 10 M Ω when filled with pipette solution. Data were low-pass filtered at 1 kHz and digitized at a rate of 10 kHz. The bath solution contained 140 mM NaCl, 3 mM KCl, 1 mM CaCl2, 1 mM MgCl2, 10 mM HEPES, pH7.41 and the pipette solution was 145 mM KCl, 5 mM NaCl, 2 mM CaCl2, 2 mM MgCl2, 3 mM MgATP, 4 mM EGTA, and 10 mM HEPES, pH7.35. A 0.2 nA stimulation was applied for 2 ms to induce action potential firing. Nifedipine at 100 nM was used through a gravity-perfusion system until reach the maximum inhibition was achieved. MDP, MDR, APD20, APD50 and APD90 were analyzed using the pclamp10 software.

QUANTIFICATION AND STATISTICAL ANALYSIS

Students t-test was performed unless specified. Data is presented as ± SD or ±SEM, and statistical significance is defined as the p < 0.05 (*) p < 0.01 (**) or p < 0.001 (***).

Figure 2H: RT-PCR Statistical comparison done by One-way ANOVA with post-hoc Tukey test; p < 0.05(.), p < 0.01(...), p < 0.001(...) Figure 3: (j-m) Immunoblot is presented as ± SD with three biological replicates. TFM data (s-t) significance was calculated using one-way Anova with Tukey's correction.

Figure 4: Respiration data is presented as ±SEM (n = 6 with two biological replicates) and significance calculated by one-way Anova with Tukey's HSD. Redox data is presented as ± SEM with n = 10 in each of three biological replicates. Immunoblot is presented as ± SD with three biological replicates. Statistical significance is defined as the p < 0.05 (*) p < 0.01 (***) or p < 0.001 (***).

Figure 5: In Figure 5C, data is shown as mean ± SD with n > 30; Significance determined by wilcoxon test; p < 0.001 (***). In Figure 5D, RT-PCR data is presented as ±SD (n = 6) and significance calculated by two-way ANOVA with Tukey's test. Flow cytometry data (Figure 5F) is presented as ±SD (n = 6). Immunoblot is presented as ± SD with three biological replicates. Statistical significance is defined as the p < 0.05 (*) p < 0.01 (**) or p < 0.001 (***).

Figure 6: Calcium Transient/Caffeine/Action potential data is obtained from two biological replicates and presented as mean ± SD (respective colored dots/area under the curve) with minimum n30 for each time point. Bar plots are presented from same data with \pm SD. Statistical significance is defined as the p < 0.05 (*) p < 0.01 (**) or p < 0.001 (***).

Figure 7: Respiration data is presented as ±SEM (n = 6 with two biological replicates) and significance calculated by one-way Anova with Tukey's HSD. Redox data is presented as \pm SD with \sim n = 36. Calcium Transient/BPM/Action potential data is obtained from two biological replicates and presented as mean ± SD (respective colored dots/area under the curve). Calcium transient with endothelin treatment n = \sim 39. APD n = \sim 57.

For gene ontology analyses, statistical significance and z-scores for the enrichment of differentially expressed genes in Gene Ontology gene sets was computed using the following method. First, the individual gene level p values were transformed to z scores using the inverse of the normal distribution, and the sign assigned by the direction of the fold change. Then, a p value was evaluated for the gene set by the Student's t-test performed for the genes inside and outside the test. p-values were corrected for multiple testing using false discovery rate (Benjamini-Hochberg) method.